Comprehensive Observations and Geostatistics of Slope Streaks within the Olympus Mons Aureole

D.E. Stillman[1*] (dstillman@boulder.swri.edu), R.H. Hoover[1], H.H. Kaplan[2], T.I. Michaels[3], L.K. Fenton[4], K.M. Primm[5]

[1] Department of Space Studies, Southwest Research Institute, Boulder, USA
[2] NASA Goddard Space Flight Center, Greenbelt, Maryland, USA
[3] Space Science and Engineering Center, Univ. of Wisconsin – Madison, USA
[4] SETI Institute, Mountain View, CA, USA
[5] Planetary Science Institute, Tucson, AZ, USA

*Corresponding author

Submitted to: Icarus

Initially Submitted: Sept 28, 2023
Revision Submitted: Mar 1, 2024

Highlights:

- This slope streak site exhibits the largest documented formation and fading rate ever recorded.
- Seasonal variation in slope streak formation rate displays difference of approximately sixfold.
- The observations of slope streaks at this site are consistent with the wind-triggered dry avalanche hypothesis.

Abstract

Slope streaks (SS) are enigmatic linear features characterized by relatively low-albedo features that appear and fade on high-albedo slopes on Mars. Despite numerous hypotheses proposed to explain their formation, the primary mechanism behind SS remains elusive. Here, we examine 702 SS features using 32 multitemporal Context Imager (CTX) images and mesoscale modeling data obtained from a site (centered at 31.230°N, 216.281°E) in the Olympus Mons Aureole region. Our investigation revealed several key findings that shed light on the dynamics of SS formation and fading. We discovered a significant preference for SS formation on south-facing (equator-facing) slopes compared to north-facing slopes, with SS being over seven times more likely to occur on the former. Furthermore, SS formation was found to be seasonal with significantly enhanced by a factor of ~6 near the equinoxes (from solar longitude L_s 337°–42° and 136°–227°) compared to other times of the year. Our analysis also revealed a correlation between the rates of SS formation and fading, with scree slopes exhibited the fastest-fading SS also experiencing the highest rates of newly-formed SS. Additionally, we measured the median starting and stopping slopes of SS to be 23.4° and 14.9°, respectively, significantly below the angle of repose of sand. These low slopes suggest the necessity for an energetic trigger mechanism to initiate SS formation. Infrared spectroscopy revealed that the principal distinction between the material inside and outside of a SS lies in the reduced abundance of dust within the streak. Notably, this site demonstrates the highest rates of SS formation (a 29.6% increase in new SS per Mars year) and fading (a 12% fading of SS per Mars year) ever quantified. These elevated rates may be attributed to the site's topography, which facilitates calm surficial nighttime winds throughout the year, leading to widespread dust deposition. Daytime downhill winds near the ridgelines of S-facing slopes may then trigger movement of newly deposited dust aggregates or alternatively, a Knudsen pump phenomenon could serve as a potential trigger for SS. We propose that SS is inhibited during the northern summer solstice season due to the relatively clear aphelion atmosphere, which limits dust deposition. Similarly, the lack of triggering activity during the winter solstice is likely due to more moderate daytime winds. Overall, our findings are consistent with the wind-triggered dry avalanche hypothesis as a plausible explanation for SS formation.

1. Introduction

Slope Streaks (SS) are prominent features on Mars, characterized by their relatively low-albedo and large dimensions, extending up to several kilometers in length and up to 200 m in width. These enigmatic features are observed on slopes within dusty, high-albedo, and low-thermal inertia regions from 15°S to 45°N latitude (e.g., *Sullivan et al.,* 2001; *Bhardwaj et al*., 2019). SS represent one of the few active geologic processes on the surface of Mars. While some SS have persisted for >15 Mars years (e.g., *Schorghofer et al.,* 2007; *Schorghofer and King*, 2011; *Bergonio et al.,* 2013), many SS exhibit complete fading on shorter timescales (*Dundas*, 2020). Interestingly, SS fading and formation appear unaffected by planet-encircling dust events (*Bhardwaj et al.,* 2019).

Despite their prevalence, the mechanism behind SS formation remains elusive. While triggering events such as rock falls (*Chuang et al.,* 2007; *Heyer et al.,* 2020), dust devils (*Malin and Edgett*, 2001; *Schorghofer et al*., 2007; *Heyer et al.,* 2020), and meteoroid impacts (*Chuang et al.,* 2007; *Burleigh et al.,* 2012; *Heyer et al.,* 2020) have been proposed, they account for only the minority of SS occurrences (*Heyer et al.,* 2020; *Dundas*, 2020). The absence of identifiable triggers for most SS challenges existing models, leading to theoretical explanation categorized as dry (*Morris*, 1982; *Sullivan et al.,* 2001; *Schorghofer et al.,* 2002; *Baratoux et al.,* 2006, *Phillips et al.,* 2007; *Chuang et al.,* 2007; 2010; *Dundas*, 2020) and wet models (*Ferris et al.,* 2002; *Miyamoto et al., 2004; Kreslavsky and Head,* 2009; 2019; *Mushkin et al.,* 2010; *Yakovlev*, 2010; *Bhardwaj et al.,* 2017). See *Bhardwaj et al.* (2019) for a detailed review of these models. In general, dry models struggle to explain: (1) the absence of debris accumulation; (2) the ability of granular flows to start on angles that are likely less than the angle of repose; and (3) the flow mechanism that allows granular flows to traverse hundreds of meters on shallow slopes (<20°) (*Bhardwaj et al.,* 2019). Conversely, wet models must account for: (1) the lack of SS formation seasonality during warmer periods; (2) how water alteration via hydration or altered mineralogy is suppressed in SS (*Bhardwaj et al.,* 2019); and (3) how the volume of water required to form a SS on a cold and dry planet is released.

In this study, we investigate the behavior of all the 701 SS over a ~28.56 km wide by 40.28 km long (1336 km^2) area within the Olympus Mons Aureole (OMA) region using multi-temporal observations from the Context Camera (CTX; *Malin et al.,* 2007; *Bell et al.,* 2013) onboard Mars Reconnaissance Orbiter (MRO) spanning from Mars Year (MY) 28 to 36. By analyzing SS

formation and fading rates, starting and stopping slope angles of SS, the mean slope angle of the SS, and SS density variations over the geographical area. Furthermore, we examine mineralogical signatures obtained from the Compact Reconnaissance Imaging Spectrometer for Mars (CRISM onboard MRO; *Murchie et al.,* 2007). Additionally, mesoscale atmospheric modeling is employed to refine our understanding of the seasonal environment surrounding SS.

Our overarching objective is to gain deeper insights into the lifecycle of SS and to put forward hypotheses regarding their formation mechanisms. By addressing existing ambiguities, our research endeavors to lay the groundwork for future in-depth modeling and observational studies aimed at unraveling the mysteries surrounding these intriguing Martian features.

2. Background

2.1 Site Geology

We chose to expand a previously documented SS site at 31.230°N, 216.281°E within the OMA (*Brusnikin et al*. 2016; *Heyer et al.,* 2019). This region is characterized by overlapping dust-covered sheets of uncertain origin, featuring scarps ranging from tens to hundreds of kilometers in length (*Morris and Tanaka*, 1994). Additionally, these deposits exhibit parallel ridges and troughs with rugged faulted terrain, where talus slopes provide the substrate for SS formation (*Morris and Tanaka*, 1994). The OMA has been interpreted as an apron unit containing landslide and gravity-spreading deposits, estimated to be of Amazonian age (*Tanaka et al.,* 2014). Our survey site is situated at the boundary between the lower and middle OMA units (*Morris and Tanaka*, 1994), with the lower unit clearly underlying the middle unit. This location provides a unique opportunity to study the lifecycle of SS within the context of the complex geological history and structure of the OMA region.

2.2 Slopes and Aspect of Slope Streaks

The angles at which SS start and stop play a crucial role in understanding their formation mechanism. The static angle of repose, indicating the slope angle at which granular flow begins, has been measured to be ~33° on a Martian sand dune (*Ewing et al.,* 2017). The dynamic angle of repose, representing the slope angle which a momentumless flow ceases, has been measured to range from 28 to 29.8° (*Atwood-Stone and McEwen*, 2013; *Ermakov et al*., 2019; *Ewing et al*., 2017).

Sullivan et al. (2001) conducted quantitative granular flow modeling for SS, treating them as dry dust avalanches. Their modeling assumed an initial slope of 40° for 10 meters, which then decreased to 33° over and additional 70 meters. Subsequently, the flows decelerated further as the slope angle reduced to 25° over 280 meters before almost immediately halting when the slope decreased to 5°. In contrast, *Miyamoto et al.* (2004) utilized a fluid-dynamics model to demonstrate the formation of anastomosing SS with slope angles ranging from 5 to 20° and randomly distributed 1-2 m mounds. Their finding suggested that SS could form either through water-related flow with a solid content of less than ~20% or through dry grain flows with extremely low cohesion and friction angles, supported by dispersive pressure or a lubricant.

The arrival of MRO enabled stereo imaging using the High Resolution Imaging Science Experiment (HiRISE; *McEwen et al.,* 2007), allowing *Brusnikin et al*. (2016) to extract topographic information along SS profiles. Their analysis of ~1500 SS at 19 sites revealed a range of upper (top 10-30 m segments) slopes angles (10-40°) with a median upper slope of 25.9°. The ending segment of SS exhibited angles ranging from 0 to 34° with a median of 14° (*Brusnikin et al*., 2016). These observations led *Brusnikin et al*. (2016) to suggest that SS could only start at angles steeper than ~18-20°.

Heyer et al. (2019) mapped the aspect/orientation of thousands of SS at six sites. Note that the orientation was calculated from the start to the end of the SS. Their analysis recorded a dominant SS orientation, with some sites showing a secondary orientation typically offset by 180° from the dominant one. At our survey site, they identified 475 preexisting SS and 60 new streaks with a dominant orientation between 110-210° or east-southeast to south-southwest. Previous research indicated that OMA sites with a latitude >30°N predominantly exhibit a southward orientation (*Schorghofer et al.,* 2002; *Baratoux et al.,* 2006).

2.3 Slope Streak Formation and Fading Rates

The seasonal rate at which SS form and fade are important factors to help quantify the mechanism that forms and erases SS. SS formation rate q has been previously calculated using $q = \frac{\Delta n}{\Delta t\, n}$, where Δn is the number of new SS, Δt the time interval between the two images, and n is the number of preexisting SS (*Aharonson et al.,* 2003). The formation rate at our SS monitoring site was previously measured to have a 5.5% increase in the number of SS per Mars

Year (MY; *Heyer et al.,* 2019). This is within the measured formation rate range of 2–12% per MY for all previously measured SS sites (*Aharonson et al.,* 2003; *Schorghofer et al.,* 2007; *Bergonio et al.,* 2013; *Heyer et al.,* 2019).

Fading can be difficult to assess, as changes in lighting and image quality can affect the ability to detect a nearly fully-faded SS (*Bergonio et al.,* 2013; *Chuang et al.,* 2010). The fading rates described in the literature suggest long fading time scales, with *Bergonio et al.* (2013) finding that no SS faded over ~5.3 MYs, but 74% of SS fade over ~17 MYs. Similarly, *Schorghofer et al.* (2007) found 5 of 86 SS (5.8%) faded over more than 14.1 Mars years at an OMA site (28°N, 212°E). *Schorghofer et al.* (2007) also found no SS fading of 54 SS over 6 sites with 54 mapped SS outside OMA over 13.6-14.6 Mars years. Conversely, *Dundas* (2020) found that SS fade on much shorter timescales (many SS fade quickly in <1 MY) than the multidecadal intervals reported previously. Understanding what mechanism causes such varying properties at SS sites serves as motivation for this paper. Overall, the formation rate of slope streaks is inferred to be similar to the fading rate, as the slopes which SS are formed upon are never absent of SS (e.g., *Schorghofer et al.,* 2007; *Bergonio et al.,* 2013).

2.4 Slope Streak Seasonality

The initial investigations into the seasonality of newly-formed SS revealed no correlation with Martian seasons, and SS formation was found to be unrelated to large regional events, including planet-encircling dust events (*Schorghofer and King,* 2011; *King et al.,* 2010). However, a subsequent study by *Heyer et al.* (2019) concluded a preferential formation of SS around L_s 180-270° at our study site, as well as four other OMA sites, and a site in Nicholson crater. Conversely, SS were less likely to form during L_s 0-90°. At our survey site, *Heyer et al.* (2019) proposed a seasonality enhancement factor ranging from 2 to 10 compared to the diminished season.

Furthermore, bursts of SS activity or streak showers have been observed. For example, at site 3 in *Dundas* (2020), 38 SS formed over ~3.5 Mars years, but only five formed over the next ~2 Mars years, representing a five-fold decrease in new SS activity. At a different site, *Dundas* (2020, in Extended Data Figure 1) illustrated a significant amount of SS fading and new SS formation between two images captured less than a Mars year apart, followed by no fading and only a few new SS in the subsequent image acquired almost three Mars years later.

Overall, long-term multitemporal monitoring suggests SS formation may exhibit seasonal enhancements, with annual formation rates potentially increasing over multi-year periods. Additionally, the fading rates of SS may display episodic behavior.

2.4 Mineralogy of Slope Streaks

Investigating the mineralogy of SS and their surrounding slopes is important for determining whether water alteration has occurred, which is key to support wet-based hypothesis of SS formation. Previous hyperspectral analyses of CRISM data suggest that both SS and the slopes surrounding darkened SS are dominated by ferric oxides (FeOx; *Mushkin et al.,* 2010). Additionally, it has been observed that dark SS are not associated with any water, ice, or hydration bands (*Mushkin et al.,* 2010; *Amador et al.,* 2016; *Kaplan et al.,* 2023). *Mushkin et al.* (2010) interpret the darkening of SS to be the results of staining by a silica coating, amalgamated clusters of nanophase FeOx, and/or precipitated low-albedo FeOx caused by the alteration of a brine. At a global scale, regions with a higher abundance of SS may be correlated with higher iron and chlorine abundances, as well as water-equivalent hydrogen measured with the Gamma Ray Spectrometer (*Bhardwaj et al.,* 2017).

2.5 Environment of Slope Streaks

To better characterize the mechanisms controlling SS formation and fading, it is necessary to investigate the environment conditions (e.g., surface temperature, wind speed and direction, and frost abundance and time of day) in which they occur. *Heyer et al.* (2019) modeled incoming solar radiation (insolation) for a 25° slope in a SE-facing orientation for our survey site. They found that maximum insolation, a proxy for maximum surface temperature, occurs at L_s ~170°, with a minimum at L_s 265°, and relatively high levels between L_s 10°–190°. Notably, maximum formation rates appear to correlate with the maximum insolation (*Heyer et al.,* 2019).

To estimate the wind field at our OMA survey site, *Heyer et al.* (2019) utilized data from the Mars Climate Database version 5.3 (MCD; *Forget et al.,* 1999; *Millour et al.,* 2015). However, it is important to note that these data provide a general indication of regional winds, as the MCD does not fully account for local and regional topography (*Martínez et al.,* 2017). *Heyer et al.* (2019) interpreted daytime-maximum near-surface wind intensity at a height of 2 m above the surface. They found that at our survey site, peak wind speed reached ~17 m/s at L_s ~180°, with a

minimum of ~10 m/s at L_s 270°, and moderate winds of ~12 m/s from L_s 0°–100°. Interestingly, the highest formation rates appear to correlate with periods of maximum of daytime-maximum near-surface wind speed (*Heyer et al.,* 2019).

Baratoux et al. (2006) employed a Global Climate Model (GCM) to estimate the regional wind field at a spatial resolution of 2° by 2° and an altitude of 50 m. They averaged wind directions and intensities over a period of 10 days at the dustiest time of the year (L_s 255°). They argue that during the season of maximum dust deposition, the preferred SS orientations correlated with downhill wind directions that trigger SS activity.

Furthermore, SS are observed on high-albedo dusty surfaces with low thermal inertia (*Ferguson and Lucchitta,* 1984), which often experience very low surface temperatures before sunrise. These cold temperatures may facilitate the formation of CO_2 frost within the subsurface (*Piqueux et al.* 2016; *Lange et al.,* 2022), which would quickly sublimate immediately after sunrise as temperatures rise. This CO_2 frost formation would be more favorably on colder, pole-facing slopes during the coldest parts of the year.

In summary, SS formation has been suggested to be influenced by factors such as enhanced insolation, increased downslope wind speeds, and the sublimation of CO_2 frost.

2.6 Dry Avalanche Slope Streak Mechanism

Dry, wet, and hybrid SS trigger mechanisms were recently reviewed by *Bhardwaj et al.* (2019). Here, we expand on the dry dust avalanche mechanism, which can be triggered by various events such as impact cratering, rockfalls, marsquakes or dust devils. However, for SS without an apparent trigger, high winds are likely the cause (*Dundas,* 2020). Wind speeds have been implicated in SS seasonality (*Heyer et al.,* 2019), and occasional bursts of formation can be attributed to stochastic high-wind events, which can also rapidly fade existing SS (*Dundas,* 2020). *Baratoux et al.* (2006) suggests that the rate of dust accumulation may be controlled by wind direction and speeds around obstacles, with accumulation occurring on the lee side of ridges followed by failure via oversteepening.

Additional factors contributing to SS triggering events include electrostatic effects of dust (*McEwen et al.,* 2019; *Dundas,* 2020) and thermal creep by insolation processes (*Schmidt et al.,* 2017; *Dundas,* 2020), which are strongest in fine-grained material. Temperature changes may also impact soil hydration and cohesion (*Gough et al.,* 2020). Modeling by *Sullivan et al.* (2001)

demonstrated that dust avalanches triggered on a 40° slope accelerates down the slope, entraining more material and widening its front. This increase in mass and speed results in greater kinetic energy, leading to a significant portion of dust being lost to the atmosphere via suspension (*Sullivan et al.,* 2001). The loss of dust to the atmosphere was modeled to be 89-99% of the total mass (*Sullivan et al.,* 2001). This significant loss of dust explains why terminus deposits are absent in SS.

The gradual fading and erasure of SS are commonly attributed to the accumulation of dust, which eventually covers the topographic surface roughness generated by the initial flow (*Phillips et al.,* 2007; *Chaung et al.,* 2007; 2010; *Schorghofer et al.,* 2011; *Valantinas et al.,* 2021).

2.7 Recurring Slope Lineae (RSL) Compared to Slope Streaks

RSL share similarities with SS as they both appear as low-albedo lineations descending steep slopes. Proposed formation mechanisms of RSL include wet, dry, and hybrid mechanisms, similar to those proposed for SS. Dry RSL mechanisms involve phenomena such as dust avalanching (*Schaefer et al*., 2019; *Vincendon et al.,* 2019), akin to the SS mechanism proposed by *Sullivan et al.* (2001). However, RSL occur on much steeper slopes (*Dundas et al.,* 2017; *Stillman et al.,* 2020), and they exhibit incrementally lengthen, rapid fading (much less than a Mars year), and recur on a yearly or bi-yearly cycle (*Stillman and Grimm*, 2018). Moreover, RSL are typically much smaller in size (~100 m in length) compared to SS, and they tend to be located in areas with less dust accumulation (*McEwen et al.,* 2011; *Stillman*, 2018). Notably, RSL greatly enhanced by planet-encircling dust events (*McEwen et al.,* 2021), while SS are not affected by such events (*Bhardwaj et al.,* 2019).

2.8 Remote Sensing Data

CTX images, with a resolution of ~6 m, have been acquired since Nov 8, 2006 or MY 28 L_s 132.2°. Our analysis utilized all CTX images acquired prior to June 1, 2022 or MY 36 L_s 238.2°. Using JMARS (Christensen et al., 2009), we identified overlapping CTX data frames covering our study site. Subsequently, these frames were downloaded as Pyramidized TIFs and imported into ArcMap 10.8.1 (software from Esri®), for further processing and analysis.

CTX stereo pairs within our study area were identified and utilized to generate a digital elevation model (DEM) with a resolution of 8.5 m per pixel. Initially, CTX images were

downloaded as TIFs and processed using standard CTX processing techniques in Integrated Software for Imagers and Spectrometers (ISIS). This encompassed conversion of the files to ISIS compatible .cub files, incorporation of SPICE information (*Acton*, 1996), radiometrically calibration, and removal of even/odd detector striping. Subsequently, the processed images were utilized in the Ames Stereo Pipeline (ASP) (*Beyer et al.*, 2018) software to create a point cloud , which was further transformed into a DEM. We determined that the More Global Matching (mgm) algorithm produced the highest-quality DEM for our survey site. The DEM was aligned with MOLA shot values using the pc_align tool. Upon integration into ArcMap, the DEM facilitated the extracted of elevation values of each SS, utilizing various tools discussed in §*3.2*. Additionally, the DEM served as an input for the mesoscale atmospheric modeling discussed in §*3.5*.

3. Methodology

3.1 Slope Streak Mapping

Using ArcMap 10.8.1, we mapped all the SS within the study area by analyzing all overlapping CTX images. The SS were delineated with a polyline tracing down the central axis of each SS. Note that SS occasionally bifurcate as they descend downslope. In such cases, we measured the spine of the longest split. We recorded the formation, fading, overprinting, or when SS were not imaged in our supplementary data (**OM_A_edits_030124.xlsx**). The latter occurs in some CTX images because of incomplete coverage of the study area. Since the CTX images were not orthorectified, we focused on mapping SS on CTX images that had emission angles close to 0° (**Table S2**).

Identifying newly-formed SS is relatively straightforward due to their distinct albedo contrast, although they can be mistaken for shadows. Therefore, before mapping SS, we ensured that these streaks remained static as the shadows changed with the seasons. Conversely, detecting fading SS is more subjective, as they gradually fade over multiple Mars years, and changes in lighting and image quality can affect their visibility (*Bergonio et al.*, 2013). Moreover, nearly-faded SS in the initial CTX images were not mapped if they were not clearly identifiable as SS, as it was uncertain whether they were actual SS or simply albedo patterns on scree slopes. Our fading database is biased towards capturing additional fading over time, as it is

easier to identify a previously-mapped SS in a nearly-faded state than to recognize an unmapped SS in a faded state.

To calculate fading statistics, we excluded existing SS from the first CTX image, as their formation dates could not be determined. We then calculated the time period between the cessation of SS (extending from the last image with the SS to the first image without the SS) and their starting date (extending from the last image without the SS to the first image with the SS). This provided an estimate of the duration for which the SS existed on the surface of Mars. The uncertainties associated with fading statistics are significantly higher than those for seasonal starting SS statistics due to the uncertainty in both the formation and fading times, exacerbated by the cadence of the CTX images. Additionally, determining the exact point at which a SS fully fades is more challenging than identifying its formation due to various factor such as lighting conditions and image quality.

3.2 Slopes and Aspect

The positional data for the SS polylines, including northings, eastings, and elevations, was exported using ArcMap's Data Management tools (*Generate Points Along Lines* and *Extract Values to Points*). Utilizing *Generate Points Along Lines*, we generated points at 8.5 m intervals along each SS mapped as a polyline. Employing *Extract Values to Points*, we captured the elevation value at each point along the slope streak. This data, comprising location and elevation, was compiled into an elevation file and imported into MatLab for calculating slope geostatistics and orientations. The starting orientation of each SS was calculated based on its orientation over the first 5 data points, corresponding to a length of 34 meters.

In computing the slopes of the SS profiles, we identified and omitted profiles located in sections of the DEM exhibiting inconsistent data, typically arising from instances where the ASP algorithm failed to generate a satisfactory solution. This resulted in the exclusion of 62 out of the 702 initially mapped SS. Starting and stopping slopes were computed as the mean and standard deviation over the initial and final 5- and 6-data points, respectively, with each data points separated by an 8.5 meter interval. Profiles with standard deviations exceeding 10° were excluded due to excessive error. We also examined the difference in computed mean slope values for the 5- and 6-data segments, excluding slopes with a difference greater than 4°. The

chosen 5- or 6-data point mean slope value was selected based on the method producing the lowest standard deviation. This vetting process excluded 44 starting and 23 stopping slopes.

Using ArcMap, we delineated polygons over regions featuring slopes within the 75% most likely values derived from our computed starting slope value. These polygons were further classified based on orientation (NW- or SE-facing slopes) and their position within the middle or lower OMA geologic unit. Subsequently, we quantified the SS count initiating within each polygon, normalizing by the ArcMap-generated area of the respective polygon. This facilitated the determination of SS density for both the first and last CTX images covering the entire study area, along with the densities of newly-formed and faded SS. Areas smaller than 0.4 km^2 were excluded from the analysis to precent disproportionate influence on SS density calculations, reducing the total mapped area by 10%.

3.3 Seasonality

To quantify seasonality, we constrained the dates of newly-formed SS by leveraging sequential CTX images that captured their formation (e.g., *Aharonson et al.,* 2003; *Schorghofer and King,* 2011; *Stillman et al.,* 2014). We calculated the newly formed rate R_{Obs} as a function of the sol of the Mars year using the formula:

$$R_{Obs}(sol) = \frac{N_{ObsNewSS}}{\Delta t} A_{NewSurveyArea}, \quad \text{(Eq. 1)}$$

where $N_{ObsNewSS}$ represents the number of newly formed SS, Δt denotes the number of sols between the CTX image pair, and $A_{NewSurveyArea}$ signifies the newly imaged percentage of the survey area of the CTX image pair. Note that R_{Obs} is also a function of Δt, with a larger temporal threshold allowing for more CTX image pairs, albeit with a blurred temporal resolution of when newly formed SS occurred. Additionally, $A_{NewSurveyArea}$ will be 100% for CTX images that fully cover the survey area. However, only 15 out of the 32 CTX images cover the entire survey area. For example, if the first CTX image covers the entire image, but the subsequent image covers only 75%, then $A_{NewSurveyArea} = 75\%$. Subsequently, if a third CTX image then covers the remaining survey area, then $A_{NewSurveyArea} = 25\%$. The areal coverage of each CTX image was measured in ArcMap (**Table S2**). The value of R_{Obs} is computed for each image pair at every sol of the Mars year. Subsequently, these data points are summed, and R_{Obs} is normalized

by this cumulative sum. This normalization process allows us to estimate the percentage of newly formed SS observed to occur at each sol of a Mars year P_{Obs}.

Our assessment of the observed percentage of newly formed SS is subject to bias due to the non-uniform acquisition of CTX images across the Mars year. To demonstrate this bias, we devised a model to calculated the rate of newly formed SS $R_{Model}^{Uniform}$ as follows:

$$R_{Model}^{Uniform}(\text{sol}) = \frac{NormRate}{\Delta t} A_{NewSurveyArea}. \quad \text{(Eq 2)}$$

In this model, we utilize the same CTX image pairs and $A_{NewSurveyArea}$, while assuming a uniform SS formation rate $NormRate$ over the entire Mars year. Similar to P_{Obs}, the value of $R_{Model}^{Uniform}$ is computed for each image pair at every sol of the Mars year. Subsequently, these data points are summed, and $R_{Model}^{Uniform}$ is normalized by this cumulative sum. This normalization process allows us to estimate the percentage of SS formed at each sol of a Mars year $P_{Model}^{Uniform}$, assuming uniform SS formation across the entire Mars year.

To better characterize the uncertainty in $P_{Model}^{Uniform}$, we conducted a simulation to estimate the expected number of SS formed over the number of sols between the CTX image pairs. Using a Poisson distribution, we computed the probability of the number of SS that would form over the same number of sols between the CTX image pair. Subsequently, we utilized a random number generator to determine a value for the number of modeled SS to use for each CTX image pair. Following this, we calculated the normalized percentage of modeled SS for each sol of the Mars year. This simulation process was repeated 10,000 times to generate statistics. The mean of the simulations equaled $P_{Model}^{Uniform}$, and the standard deviation was determined to estimate the error for each sol of the Mars year.

We proceeded to compare our observed formation rates to the uniform modeled formation rates across various temporal threshold in sols. To quantify the magnitude of seasonality, we calculated the ratio between P_{Obs} and $P_{Model}^{Uniform}$. These values were then normalized by dividing by the mean of the all the seasonal values, allowing the mean normalized formation rate to equal unity. This normalization enabled us to interpret seasons with enhanced formation (observed rates > modeled rates), diminished formation (observed rates < modeled rates), and periods with no data (no CTX image pairs). To quantify the statistical significance of the seasonality, we calculated the difference between P_{Obs} and $P_{Model}^{Uniform}$ divided by the standard deviation for each

sol of the Mars year. This provided us with the number of standard deviations for each sol of the Mars year. Similarly, we calculated the difference between P_{Obs} and $P_{Model}^{Uniform}$ divided by $P_{Model}^{Uniform}$ to determine the magnitude of the enhancement (>1) or diminishment (<1). Subsequently, we determined the mean and standard deviation of each interpreted season in terms of the number of standard deviations and the normalized magnitude of seasonality.

In addition, for comparison with previous works, we calculated the ratio of new and faded SS to the number of existing SS, as originally outlined by *Aharonson et al.,* (2003). We only used the CTX images that had 100% coverage to avoid statistical complexities, except in one case. CTX image D07_029888 covers 99.3% of the study area; however, we know from subsequent images that no SS faded or formed in the 0.7% of the area missed by the image. We utilized this image to compare to the statistics reported by *Heyer et al.* (2019). Thus, we compare incremental ratios and ratios over our entire monitoring period, as well as the monitoring period used by *Heyer et al.,* (2019).

3.4 Infrared Spectroscopy

We analyzed two CRISM images that covered part of the survey site (frs0003d33a and frs0003005c) using the Environment for Visualising Images (ENVI) processing software. We used the CRISM Analysis Toolkit (CAT) to correct observations for illumination conditions and atmospheric gas absorptions. Visible-near-infrared (VNIR) and infrared (IR) datasets have been co-registered to provide a continuous spectrum from ~0.4 to 3.9 μm. We collected spectra from averaged pixels acquired over each slope streak in the CRISM images. We ratioed the slope streak spectra to two different background spectra to emphasize spectral variations; for background material, we used a spectrum of a dusty region collected from within the same image and a spectrum from the nearby slope.

3.5 Mesoscale Climate Modeling

Orbital remote sensing data of surface temperatures and other atmospheric quantities have limitations, as they generally provide only snapshot of environmental conditions twice a day, and most atmospheric quantities are not observed within ~10 km of the surface. To comprehensively estimate the near-surface environment relevant to SS evolution at our study area, we performed

high-resolution climate simulations with the Mars Regional Atmospheric Modeling System (MRAMS; *Rafkin et al.,* 2001; *Rafkin and Michaels,* 2019).

Our OMA study site (see §2.1) presents a complex topographic setting for atmospheric modeling. To balance resolving the most important aspects of the numerous ridges/valleys at this site with the computational demands of simulating the atmospheric flow/state over an area somewhat larger than our study site, we utilized a series of eight nested MRAMS grids. Each grid had successively smaller total area and horizontal grid spacing, ultimately achieving the desired horizontal grid spacing of ~400 m over the study site. This approach also allowed us to capture important relevant regional circulations, such as flow towards or away from Olympus Mons and the greater Tharsis plateau. We used a combination of the blended MOLA-HRSC global DEM (*Fergason et al.,* 2018) and our CTX-derived DEM to provide the necessary topographic data for our simulations.

Given the significant computational effort required for each simulation, MRAMS runs, each 2 sols in duration, were performed for four canonical seasonal L_s windows, centered on L_s 10º, 100º, 190º, and 280º, to explore seasonal variability. Output from the NASA Ames Research Center Mars Global Climate Model (MGCM; *Haberle et al.,* 2019) with ~300 km horizontal grid spacing, was used to provide the initial state and time-dependent lateral boundary conditions for the MRAMS runs. Snapshots of the 3-dimensional MRAMS model state (atmosphere and surface/subsurface) were recorded every 10 Mars-minutes, and the last sol of each run (to avoid model spin-up effects) was then further investigated using a variety of visualization and analysis strategies. Preliminary results showed that a one-sol MRAMS spin up was sufficient due to the low thermal inertia of the survey site, allowing surface temperatures to quickly respond to higher resolution topographic slope angle effects.

Utilizing the output from MRAMS models, we extended our analysis to determine the dust fall speed w for dust grains with a radius of 5 μm and a density of 2700 kg/m^3 (*White et al.,* 1997). Additionally, we computed the friction velocity u^* (*Kok et al.,* 2012). Lastly, we estimated the likelihood of suspension or deposition by computing a ratio of u^*/w, where a ratio greater than 7 indicates suspension of a dust grain 5 μm radius (*White,* 1979; *White et al.,* 1997).

4. Results and Interpretations

4.1 Geologic Setting and Slope Aspect

We concentrated our SS mapping efforts on an OMA site centered at 31.230°N, 216.281°E (**Fig. 1**), utilizing 32 CTX images that partially to fully covered the area of interest (**Table S1-S3**). While this site had been previously mapped by *Heyer et al.*, (2019), we extended their mapping efforts by incorporating an additional 18 new partial CTX images. Our mapping effort revealed a total of 215 SS in the first image, with a cumulative count of 702 SS over all the images.

Situated at the contact between the lower and middle OMA units (*Morris and Tanaka*, 1994; **Fig. 2**), the study site presents a distinctive geological setting characterized by parallel ridges within the middle OMA unit. These ridges feature extensive areas of steep slopes, primarily oriented in NW- and SE-facing orientations. The lower OMA unit is lower in elevation, with smaller and less-continuous slopes than the middle OMA unit. Notably, the middle OMA unit's parallel ridges harbor the majority of SS occurrences across the site (**Fig. 2**). However, SS distribution is asymmetric, with predominant presence on the SE-facing slopes within an aspect range of 67.5 – 225° (clockwise from north). A smaller population of SS is also found on NW-facing slopes with an aspect range of 270 – 360° (**Fig. 3**). Note, that our measurements of SS orientations were conducted along the initial 34 m of each SS, rather than along the entire SS length, as was performed by *Heyer et al.* (2019). The modification was made to focus specifically on the mechanism triggering the SS formation, as the calculation of orientation along the entire length is complicated by changes in slope orientation along the path of the SS.

4.2 Slope Streak Slope Angles and Areal Density

We found median starting and stopping slopes for SS of 23.4° and 14.9°, respectively, a result comparable to the findings of *Brusnikin et al*. (2016), who reported median starting and stopping slopes of 25.9° and 16°, respectively (**Fig. 4**). Less than 2% of SS exceeded the expected static angle of repose of 33° (*Ewing et al.*, 2017). We observed that orientation does not significantly affect the angles of the starting and stopping slopes. Furthermore, we found no correlation between traverse distance and either the starting slope or the entire averaged slope (**Figs. S1-S2**). While stopping slopes decreased with increasing traverse distance (**Fig. S3**), this

difference lacked statistical robustness and may simply be attributed to longer SS extending to less-sloped topography.

Utilizing our starting slope database, we determined that 75% of the starting slopes fell within a range of 15.6° to 29.5° (**Fig. 4**). Subsequently, we mapped the area of slopes within 75% of the starting slopes (**Fig. S4**), categorized as either SE- (from 67.5 – 225°) or NW- (from 270 – 360°) facing (**Fig. S5**; **Table 1**). Although the geomorphology of the slopes in both units yielded similar areas for SE- and NW-facing slopes, SS within the middle unit were noticeably more concentration on SE-facing slopes compared to NW-facing slopes (**Table 2**). Calculating the SS density by dividing the number of SS by the area revealed that SE- and NW-facing slopes had SS densities ranging from 2.3 – 3.1 and 0.14 – 0.46 SS per km^2, respectively, in the middle OMA unit (**Table 2**). Consequently, there was an approximately an order-of-magnitude (factor of 6.8 to 16.4) enhancement of SE-facing SS density compared to NW-facing SS density (**Table 2**).

We then investigated the geographic variability of the SS density (**Figs. 5-8, S6-S7**). Notably, the density of all mapped SS was greatest along the large continuous ridges in the middle OMA unit (**Fig. 5**). For instance, the NW-facing slope of the labeled ridge in **Figure 5** ("Long Continuous Ridge") exhibited an all-mapped SS density of 5.70 km^{-2}, the highest value among all mapped NW-facing area. However, this greatest value remained lower than the average all-mapped NW-facing SS densities of 8.39 km^{-2} for the middle OMA unit, indicating a significant asymmetry in SS facing orientations. Additionally, the SE-facing slope area of this ridge (**Fig. 5**) displayed a much higher all-mapped SS density of 45.13 km^{-2}, representing a factor of 7.4 increase compared to the all-mapped NW-facing SS density.

It is noteworthy that the distribution of SS density exhibits minimal geographic variation when comparing the mapped SS at MY 28.641 (**Fig. S6**) and MY 35.818 (**Fig. S7**). However, the density of existing SS did increase from MY 28.641 to 35.818 (**Table 2**). This trend may be attributed to a bias in mapping SS as existing in the latter images, where very faded SS may not have been identified in the first images. Notably, the largest densities of newly-formed SS and fading SS were observed on the same SE-facing continuous ridge located in the SE corner of the mapped area (**Fig. 6-7**). Moreover, a cross-plot of the density of faded and newly-formed SS confirms their correlation (**Fig. 8**).

4.3 Seasonality

At our survey site, we provide the CTX images (**Table S1**) and CTX image pairs (**Table S2**), as well as the L_s and sol interval (**Table S2)**, repeated coverage area percentage (**Fig. S8**), number of newly-mapped SS (**Table S2 and Fig. 9)** for each CTX pair, and the area-normalized number of CTX images for each sol of the Mars year (**Fig. S9**). Overall, a total of 702 SS were mapped within our survey site. Among these, 77 new SS formed and were captured within a sol interval threshold of 141 sols.

To discern seasons of enhanced and diminished SS formation, a comparison between the percentage of new SS formation per sol for the observed data and a modeled uniform rate was conducted (**Fig. 10a**). Furthermore, varying the sol increment was employed to ascertain the stability of the results (**Fig. 11**). We observed that for the sol of the MY intervals ranging from 27–86 and sol 626–669 transition from being enhanced to diminished as the sol interval threshold increases. Similarly, sol of the MY intervals from 448-511 exhibit a diminishment at small sol interval thresholds and enhancement at large sol interval threshold. Our interpretation of enhancement/diminishment primarily relies on the behavior observed at small sol intervals.

Overall, we observed enhanced seasons of SS formation occurring between a sol of the MY of 626–86 (L_s 337–42°) and 290–448 (L_s 136–227°), with the remainder of the year exhibiting a diminished SS formation rate. The most pronounced enhanced in formation rate occurred during the 180° equinox, registering a rate of 1.90±0.39, while the diminished formation rate during the 90° solstice is the lowest rate of 0.30±0.14 (**Fig. 10c; Table 3**). Both the 180° equinox and 90° solstice are statically robust, being 3.5±1.8 and –2.9±0.7 standard deviations away from the uniform model, respectively (**Fig. 10; Table 3**). The other enhanced and diminished seasons centered around the 0° equinox and the 270° solstice displayed one standard deviation error bars on their rates 1.60±0.50 and 0.55±0.39 that approached a uniform rate, respectively (**Table 3**). The enhanced equinox seasons cover ~43% of a MY, and the maximum seasonal variation shows that on average, there is a six-fold (with a range of 3.4 – 14.3 times) increase in SS formation during the 180° equinox compared to the 90° solstice.

The long-term newly-formed SS rates were calculated by dividing the newly-mapped SS by the number of Mars years between the interval of CTX images with 100% areal coverage of the study area. We computed three values: (1) the densely sampled monitoring period between MY 31.620 – 33.561; (2) the densely sampled monitoring period between MY 35.186 – 35.818; and

(3) the full range of the dataset of MY 28.641 – 35.818 (**Fig. 12a**). We found a rate of 31.0 and 76.3 newly-formed SS per Mars year for the densely sampled times and 64.6 newly-formed SS per Mars year for the full dataset (**Fig. 12a**), indicating a variability of over two-fold in SS activity over short durations.

Further analysis involved the computation of the anticipated count of modeled SS observable during each of the four seasons within the middle OMA unit of our study area over a single Mars year (**Table 4**). This computation incorporated the annual rate of SS formation, quantified at 64.6 SS per Mars year (**Fig. 12a**), and accounted for the SE- and NW-facing SS ratio of 7.6 (**Table 2**), normalized by the number of SS per km^2 (**Table 1**).

Additionally, we evaluated our formation rate using the methodology proposed by *Aharonson et al.* (2003), aiming to establish a comparative analysis with prior research. Notably, we observed a substantial formation rate persisting throughout the entirety of our CTX image duration, indicating a 29.6% increase in SS per MY. In contrast, *Heyer et al.* (2019) reported a rate of 5.5% per MY. However, upon reevaluation using the same images, we identified a more comparable 7.4% increase in SS per MY (**Fig. 12b**). Previous studies have quantified the increase in SS per MY, yielding varying values, such as 12% (*Aharonson et al.*, 2003; *Bhardwaj et al.*, 2017), 3% (*Schorghofer et al.,* 2007), 4.7% (*Bergonio et al.,* 2013), and 7.9% (*Heyer et al.,* 2019). It's noteworthy that our measured percentage increase in SS per Mars year, spanning the entire range of images, surpasses previously documented rates.

4.4 Fading and Overprinting

Over the entire CTX dataset, we found that 365 SS faded (**Table S2**). To estimate the fading rate of a SS, we analyzed the number of faded SS as a function of time from the first CTX image (**Fig. 13a**). We observed that SS fading follows an exponential growth pattern over the 7+ Mars year dataset (**Fig. 13a**). However, this exponential growth cannot be maintained as the newly-formed SS rate is linear (**Fig. 13a**). This discrepancy is likely due to our known bias of not initially mapping near-faded SS due to their slight albedo contrast. We also computed that the fading percentage of SS per Mars year is 12%, which is considerably smaller than the 29.6% increase in SS per Mars for newly-formed SS. This again, leads us to the conclusion that our initial SS picks lacked many SS that were nearly faded.

To determine the duration of a SS, we searched for SS that were relatively well constrained in time. Such SS have their formation and fading dates known to within $L_s \leq 144°$. Only 21 SS met these criteria, but they constrain SS duration to be between 3 and 3.8 Mars years (**Fig. 14**). However, many SS last longer than four Mars years. Thus, we calculated the ratio between dark and unfaded SS and the total number of SS (faded and dark) as a function of time, regardless of the uncertainty of their formation or fading date. We found that ~50% of SS fade within 4 to 6 Mars years of their formation (**Fig. 15**). Additionally, during mapping, we found six SE-facing SS that were overprinted before they faded. In each case, the new SS completely obscured the previous SS.

4.5 Infrared Spectroscopy

The CRISM observations at our survey site reveal repeat coverage over at least four SS, with data acquired at MY 32 L_s 135.8° and MY 33 L_s 182.1°. Among these, one SS is observed forming, while the other three maintain a similar appearance and extent over this period. Analysis of the newly-formed SS indicates a negative continuum from ~0.4 to 0.6 μm, followed by a more neutral, albeit still negative, continuum from ~0.6 to 2.5 μm (**Fig. 16**). This spectral absorption near 0.6 μm has been suggested by *Mushkin et al.* (2010) to result from an enhancement in FeOx or a silica coating. Similar features are observed in the spectra of the other three relatively unchanged SS, particularly evident in spectral ratios between streaks and nearby slopes. While one of these SS exhibits the same albedo in both images, the other two appear to have lower albedos compared to the nearby slope in the later image, suggesting at ongoing darkening over time. Notably, none of the SS spectra show evidence of liquid water or alteration minerals containing hydroxide, such as absorptions near 1.4, 1.9, or 2.1 to 2.4 μm (*Mustard et al.*, 2008), similar to findings of *Amador et al.* (2016) (**Fig. 16**). A broader investigation of SS with CRISM, including the survey area, concludes that the spectral properties of the fresh streak are consistent with dust removal from the slope (*Valantinas et al.*, 2021; *Kaplan et al.*, 2023).

4.6 Mesoscale Climate Modeling

To better understand how surface winds may influence the resetting and triggering of SS, we analyzed the wind speed and orientation at four canonical seasons (L_s 10°, 100°, 190°, and 280°) over the study site (**Fig. 17, S10-S12**), as well as three profiles (west – **Figs. S13-S17**, central –

608 **Figs. 18-20, S18-S23** and east – **Figs. S24-S27**). Our analysis revealed that daytime near-surface
609 (averaged over 0-10 m above ground level) wind speeds increase with solar insolation and are
610 predominately oriented along the profiles, roughly orthogonal to the ridges, in an approximately
611 NW - SE orientation over most of the surface (**Figs. 17, S10-12, S15, S19 & S25**). These
612 daytime surficial winds are strongest at L_s 100° (near northern solstice) and 190°, and relatively
613 moderate at L_s 10° and 280° (**Figs. 17, 19, S10-S12, S16 & S26**). However, despite their
614 strength, these daytime wind speeds results in friction velocities u^* that exceed $7w$ (where w
615 represents the fall speed of dust particles; *White*, 1979; *White et al.*, 1997; **Fig. 22**), significantly
616 reducing the likelihood of daytime dust deposition. Additionally, the NW-facing slopes of the
617 ridges and at ridge peaks experience enhanced wind speeds across all seasons (**Figs. 17, 19, 20,**
618 **S10-S12, S16, S21-S23 & S26**).
619 Notably, our results differ slightly from *Heyer et al.* (2019), who reported the strongest
620 daytime winds occurring at L_s 180° and moderate winds in the L_s 0-100° season. In contrast our
621 modeling reveals that winds at L_s 190° and 100° are both strong in intensity. This discrepancy is
622 due to the inability of MCD to resolve kilometer-scale ridge topography and resulting wind
623 speed modulations, while our mesoscale MRAMS simulations can.
624 For nighttime winds, our analysis focused on the central profile (**Figs. 17-20 & S21-23**) for
625 sake of brevity, as the interpretations of the west and east profiles are largely similar. Nighttime
626 winds prevailing above the site predominately originate from the southeast, a pattern reflected
627 across the ridgetops and many NW-facing slopes within the middle OMA unit. Conversely, on
628 the SE-facing slopes and in the interstitial valleys, the winds are notably weaker and tend to align
629 parallel to the ridges. Seasonally, nighttime surficial wind speeds peak during the SS-enhanced
630 equinox seasons. However, nighttime wind speeds at L_s 280° are only marginally weaker than
631 those at L_s 190°, while wind speeds at L_s 100° are significantly lower (**Figs. 17, 19 & S21-S23**).
632 Our modeling indicates the presence of a low-level jet above the site's southern ridges at an
633 altitude of -2000 to -1500 meters above the areoid (**Fig. 20 & S21-23**, i.e., the darker-blue
634 contours). As the ridges elevate along the profile transect, gravity flows are likely to intensify the
635 downward flow of cold, denser air, resulting in strong surficial winds down the NW-facing
636 slopes of the 3rd and 4th topographic highs (observed at along-traverse distances of 10 and 18 km)
637 along the central profile (**Figs. 20, S21-23**). However, these strong winds fail to reach the surface
638 along much of the NW- and SE-facing slopes of 5th, 6th, and 7th topographic highs, remaining

concentrated along the ridgetops (**Fig. 19**). Interestingly, the NW- and SE- facing slopes of the 3rd and 4th ridges along the central profile exhibit a low density of SS (**Fig. 18**). Conversely, at the 5th topographic high along the profile, both the NW- and SE-facing slopes have a high density of SS. Thus, there are numerous locations on the SE-facing slopes (and some of the NW-facing ones) where projected nighttime wind speeds along the profile are <5 m/s across all seasons. Towards the end of the central profile (south-southeast of the 5th topographic high and distances greater than 29 km along the transect), the topographic highs diminish in relief, experiencing relatively calm nighttime surficial winds (**Figs. 20)**.

Notably, the SE-facing slopes of the 8th topographic high exhibit the highest density of fading and newly-formed SS, despite experiencing the weakest nighttime surficial winds among the ridges in the study area. This suggests that if winds serve as the sole or primary trigger of SS, the genesis of SS is more complex than a simple correlation with high wind speeds.

5. Discussion

5.1 Geomorphological Factors, Slope Streak Density and Seasonal Variations

Our investigation at the site revealed significant differences in SS density between the SS-poor lower OMA unit and the SS-rich middle OMA unit (**Fig. 2; Table 2**). The elevation contrast between the two units, with the middle OMA unit sitting higher due to its formation atop of the lower unit (*Morris and Tanaka,* 1994), likely contributes to this disparity. Moreover, the middle unit's ridges are taller and wider, some spanning over 10 km in length, contrast with the less extensive and shorter ridges in the lower unit. Additionally, small ridges within the middle OMA unit exhibit a lower SS density (**Fig. 5**), fewer newly-formed SS (**Fig. 6**), and a decreased density of faded SS (**Fig. 7**) compared to continuous ridges. Consistent with findings of *Heyer et al.* (2019), SE- and NW-facing slopes exhibit a substantial discrepancy in SS occurrences, with SE-facing slopes being preferred by a factor of ~7.6.

Our study identified seasonal variations at the site, with an approximately sixfold increase in SS formation during equinox seasons compared to solstice seasons. However, our analysis differs from *Heyer et al.* (2019) in terms of the detected seasons of enhancement and diminishment. We interpreted a seasonal enhancement spanning from L_s 136° to 227° (180° equinox) and a seasonal diminishment from L_s 42° to 136° (90° solstice). While *Heyer et al.* (2019) reported an enhancement from L_s 180° to 270° and diminishment from L_s 0° to 90°.

Consequently, our analysis shifts the enhanced and diminished seasons identified by *Heyer et al.* (2019) by an L_s of ~45° early and later in the year, respectively.

The disparity in findings between our study and *Heyer et al.* (2019) likely stems from our use of a larger dataset, comprising of 33 image pairs documenting new SS formation and 22 pairs documenting no new SS formation (**Table S2**), compared to *Heyer et al.* (2019) use of 13 image pairs. Our expanded dataset allowed for more refined analysis of seasonalities. However, despite our comprehensive dataset, some seasons exhibited larger relative error bars and may have weaker enhancements or diminishments.

Notably, our analysis detected a seasonal enhancement spanning from L_s 337° to 42° (360° equinox) and a seasonal diminishment from L_s 227° to 337° (270° solstice). The most prominent enhancement occurred during the 180° equinox, with a formation rate of 1.90±0.39 (error is ±1 standard deviation), while the lowest diminished formation rate of 0.30±0.14 occurred during the 90° solstice (**Table 3**). Other seasons centered around the 0° equinox and the 270° solstice exhibited rates of 1.60±0.50 and 0.55±0.39, respectively, which statistically could align near the uniform rate (**Table 3**).

Interestingly, the enhancement during the L_s 180° equinox extended across all sol interval thresholds, whereas the majority of the L_s 0° equinox season was only enhanced at sol interval thresholds <~195 sol (**Fig. 11**). This suggests that the L_s 0° equinox may be shorter in duration or smaller in magnitude compared to the L_s 180° equinox enhancement.

A small streak shower (short duration bust of activity as documented in *Dundas*, 2020) of 7 newly-mapped SS was observed from L_s 182.1 – 191.5° (16 sols) in MY 33. Another possible streak shower may have occurred from 626 sol of MY 32 to 27 sol of MY 33, producing 10 newly mapped SS, with a rate more than three times higher than the nominal uniform rate (31 SS per MY from **Fig. 12**) during that time period. These observed bursts of activity do not significantly affect the seasonal analysis outside of its L_s interval. Increasing the sol interval allows additional CTX mapped pairs with less seasonal resolution to be averaged at a given sol of the Mars year. However, larger intervals provide a greater number of newly-mapped SS and are thus less influenced by short duration events (slope showers).

Overall, acquiring CTX image pairs at sol intervals <141-sols at this site and other SS monitoring sites would enhance the accuracy of SS seasonality analysis and facilitate monitoring of variances in the SS production rate, hypothesized to be influenced by PEDE activity.

5.2 Dry Formation Mechanisms

For a dry SS to form, it first must be triggered. *Sullivan et al.* (2001) modeled dry SS formation assuming a starting slope of 40° that is greater than the angle of repose. However, recent research, including our findings corroborating the work of *Brusnikin et al*. (2016), demonstrate that SS initiate on slopes well below the expected angle of repose for dry materials on Mars (*Atwood-Stone and McEwen*, 2013; *Ermakov et al*., 2019; *Ewing et al*., 2017). This discrepancy suggests that SS formation is driven by energetic processes rather than passive gravitational effects alone.

While certain energetic processes such as dust devils, meteorite impacts, and rock falls (*Malin and Edgett*, 2001; *Schorghofer et al*., 2007; *Chuang et al.,* 2007; *Burleigh et al.,* 2012; *Heyer et al.,* 2020) have been observed to trigger some SS, the majority of SS exhibit no obvious triggering mechanism. In light of this, we propose several potential mechanisms that could initiate the formation of slope streaks.

Firstly, we suggest that rapid changes in temperature could induce a Knudsen pump effect (*Schmidt et al.,* 2017). This phenomenon would significantly reduce the angle of repose by pressurizing the pore space, making the surface more susceptible to downslope movement. Fresh dust accumulation would further enhance the likelihood of the Knudsen pump phenomenon, creating conditions conducive to SS formation.

Additionally, we speculate that SS could be triggered by wind vortices that are not of sufficient strength to generate visible tracks in CTX imagery. Surface winds also could interact more vigorously with the terrain if fresh dust particles were aggregated into larger bound particles. Such dust aggregates, consisting of sand-sized particles are common on Earth (*Shao*, 2008), have been proposed to form on Mars (*Greeley*, 1979; *Bridges et al.,* 2010) and have been observed Mars-like environments in wind tunnel studies (e.g., *White et al.*, 1997; *Merrison et al.*, 2007). Furthermore, particles interpreted to be aggregates have been observed at various Mars landing sites (*Moore and Jakosky*, 1989; *Herkenhoff et al.,* 2006; *Sullivan et al.,* 2008; *Goetz et al.,* 2010; *Vaughan et al.,* 2010; *Charalambous et al.,* 2021), and may be plentiful enough to

comprise small bedforms (*Bridges et al.,* 2010). These aggregates, bonded by interparticle forces (*Greeley*, 1979; *White et al.*, 1997; *Merrison et al.*, 2004), are fragile and easily mobilized (*Shao*, 2008), making them a potential source of lofted dust on Mars.

Once triggered, granular flow along the scree slope must consist of a significant amount of dust. This dust becomes airborne and dust aggregates and particles larger than dust continue to saltate (*Bridges et al*, 2010) as the SS progresses downhill. The dust cloud then disperses quickly into the local and regional atmospheric circulations at the end of the SS flow event, explaining why no terminal deposits have been observed (*Sullivan et al.,* 2001; *Phillips et al.,* 2007).

Our investigation suggests that SS result from dry, energetic triggering processes. We propose a hypothesis regarding SS formation at our site, which revolves around the interplay of nighttime and daytime wind patterns. We theorize that SS formation at our sites is facilitated by the relatively low nighttime wind speeds over the ridges in the south and southeast sections of the study area (**Fig. 22a**). These calm nighttime conditions allow for the deposition of dust onto the surface. Subsequently, the freshly deposited dust is assumed to aggregate, forming larger dust aggregate particles (*Herkenhoff et al.,* 2006; *Bridges et al.,* 2010).

During the daytime, stronger winds in the south-southeast direction can then transport these relatively fresh dust aggregates downslope (**Fig. 22b**), particularly along SE-facing slopes. This downslope transport initiates a cascading effect, leading to a dust avalanche and the formation of SS. While both SE- and NW-facing slopes at the south-southeast end of our site receive similar amount of dust, the daytime downslope winds tend to trigger SS preferentially on SE-facing slopes. Conversely, any dust aggregates formed on NW-facing slopes may be blown upslope or even transported over the ridge onto the SE-facing slopes. This dynamic further primes SE-facing slopes for trigger events.

The absence of SS during the L_s 270° solstice season corresponds with a significant reduction in daytime wind speeds (**Fig. 19d**). Consequently, SS formation is hindered during this period due to the scarcity of a trigger mechanism. Conversely, during the L_s 90° solstice season, although strong daytime winds prevail, the amount of dust deposition is greatly reduced as the Martian atmosphere contains the lowest amount of entrained dust at this time (*Montabone et al.,* 2015). As a results, the formation of SS is limited by the diminished supply of freshly deposited dust.

The acquisition times of the CTX observations at our site do not allow us to directly determine how our SS population was affected by a planet-encircling dust event (PEDE). However, our observations do record a difference in long-term SS production of more than a factor of two (**Fig. 13a**). The slow (31.0 SS/MY) long-term SS production starts ~3 years after the MY 28 dust storm and ends just before the MY 34 PEDE. Three CTX images within ~1 MY of the end of the MY 34 dust storm show an increase in activity (76.3 SS/MY). Thus, we hypothesize that PEDEs act to recharge the SS formation system by reallocating dust, and then within a few years after the PEDE, the higher mobility of the sediment and dust enhance the formation of SS by more than a factor of two. After a few years, the mobility of the PEDE-enhanced dust and sediment decreases, and the formation rate would decrease. We suggest that CTX coverage for SS monitoring should be conducted more frequently over the next few Mars years and immediately after the next PEDE to test this hypothesis.

5.3 Fading Mechanism

Our spectroscopic analysis of SS fading cannot discriminate between the wet and dry formation mechanisms. Both processes result in darkening due dust removal and an increase in surface roughness, leading to gradual fading due to dust accumulation. The enhanced persistence of SS compared to dust devil tracks and boulder tracks implies that SS must possess greater surface roughness.

However, SS fading likely requires some form of transport to mitigate or reduce the lower albedo caused by the roughness of the SS (*Chuang et al.,* 2010). Variations in both dust accumulation and transport may explain the rapid formation and fading rate observed at our site, as well as those reported by *Dundas* (2020) and the slow formation and fading rates quantified by others (e.g., *Aharonson et al.,* 2003; *Schorghofer et al.,* 2007; *Bergonio et al.,* 2013). Further studies focusing on these variations in dust accumulation and transport (e.g., *Newman et al.,* 2005) could provide valuable insights into the dynamics underlying the formation and fading of SS.

We support the hypothesis that SS fade due to the accumulation of dust, which eventually obscures the topographic surface roughness induced by the SS (*Phillips et al.,* 2007; *Chuang et al.,* 2007; 2010; *Schorghofer and King,* 2011; *Valantinas et al.,* 2021; *Kaplan et al.,* 2023). Additionally, our observation that areas with the highest SS formation rates also had the greatest

SS fading rates (**Fig. 8**) suggests that dust accumulates more rapidly in regions experiencing above-average formation and fading. Therefore, we propose that SS formation rates depend on dust accumulation, favoring a dry SS formation mechanism.

5.4 Wet Formation Mechanisms

Our slope angle observations best align with the wet formation mechanism hypothesis. Starting slope angles that are below the angle of repose would not require an energic event for triggering, but rather a discharge of brine. Moreover, as SS progress downhill to gentler slope angles, dry flows would have little inertia to maintain their flows over kilometer scales (*Miyamoto et al.,* 2004). Conversely, SS formed via brines could continue to extend down gentle slopes (*Kreslavsky and Head,* 2009).

However, the majority of our findings do not support a straightforward wet formation mechanism, which raises several questions:

(1) Why does groundwater emerge from locations near the top of the highest ridges at the site, where the hydrological conditions are particularly challenging?

(2) Why do 12% of SS occur on the coldest NW-facing slopes?

(3) If SS are triggered by a deliquescence phenomenon, why aren't more streak showers observed when the entire survey area would experience similar favorable conditions?

(4) Why are there no signs of hydration or hydrated minerals spectroscopically?

(5) Why is fading is correlated with newly-formed SS rather than the time exposed to the sun?

While wet formation mechanisms do not require SS to start at slopes above angle of repose, they do necessitate a mechanism for discharging water on slopes that pose hydraulic challenges compared to lower elevations. However, the sloped environment can generate microclimates that may facilitate the release of brines. Despite this, SS are observed on both equator-facing (SE-facing) and pole-facing (NW-facing) slopes, with 12% appearing on the latter. Consequently, any such mechanism would need to account for the occurrence of the majority of SS on warm slopes, as well as the minority on colder slopes, characterized by higher relative humidity and frost accumulation.

The wet mechanism could potentially explain the presence of SS on pole- and equator-facing slopes via a temperature threshold that is seldom rarely obtained for the colder slopes. Such a

temperature threshold would shorten the seasonality of NW-facing SS. However, due to the limited number of NW-facing SS mapped (**Table 2**), we cannot definitively assess seasonal differences between the SE- and NW-facing slopes. To investigate this hypothesis further, a longer duration CTX monitoring survey of this site would be necessary.

CO_2 and H_2O ices likely deposit at our site (*Piqueux et al.,* 2016; *Lange et al.,* 2022; *Vincendon et al.,* 2010), but only last for a short portion of the sol and not throughout the year. H_2O ice would be more prevalent during the northern winter solstice (L_s 270°) due to colder temperature on pole-facing slopes >15° (*Carrozzo et al.,* 2009; *Vincedon et al.,* 2010). CO_2 ice could exist in low-thermal inertia regions year round, but would be more prevalent during the northern winter (L_s 270°) solstice, when temperatures are lowest (*Piqueux et al.,* 2016). However, both types of ice would preferentially form on the colder pole-facing slopes. Additionally, these ices would not form as slabs or blocks but as frost during the coldest hours of a sol. Overall, we suggest that CO_2 or H_2O frost either hampers or does not affect SS formation as ice formation peaks when SS activity is at a minimum.

The ability of salts to deliquesce H_2O out of the atmosphere and trigger SS is poorly understood (*Bhardwaj et al.,* 2017; *Gough et al.,* 2020). Laboratory experiments using large amounts of salt have been unable to measure deliquescence at low temperatures (*Fischer et al.,* 2014). Additionally, *Wang et al.* (2019) suggests deliquescence is kinetically inhibited below –20°C. While deliquescence could alter the cohesion of the regolith, the extent of this change is uncertain. If deliquescent wet flow were to occur, it remains unclear why SS would initiate from a singular point, as the entire scree slope should experience similar temperatures and relative humidities conducive to deliquescence.

If brines have been periodically flowing down these same slopes, then why are there no spectroscopic indications of hydration or hydrated minerals? While the slopes are covered in dust, recently formed SS in the CRISM data that indicate less dust coverage, but still no hydration (**Fig. 16**). Additionally, the rate of SS fading does not correlate with the duration of sun exposure, as previously hypothesized for a coating breakdown due to ultraviolent radiation (*Mushkin et al.,* 2010), but instead correlates with SS activity (**Fig. 8**; *Dundas*, 2020).

While complex wet SS formation models can address many of these questions (*Kreslavsky & Head* 2009, 2019), there remains a lack of extraordinary evidence to support these models. Nonetheless, future instrumentation such as a high-resolution synthetic aperture radar (*I-MIM*

MDT, 2022) could providing such extraordinary evidence by measuring high dielectric constants of brines in the subsurface or the polarization response of near surface ice in slope streak regions.

5.5 Slope Streaks compared to Recurring Slope Lineae

Unlike SS, Recurring Slope Lineae (RSL) start at steep slopes near the static angle of repose and stop at the dynamic angle of repose (*Dundas et al.*, 2017; *Schaefer et al.*, 2019; *Stillman et al.*, 2019). Both RSL and SS show no indications of terminal deposits, leading to the proposition of dry dust avalanches for RSL formation. However, RSL are much smaller in surface area compared to SS and at the resolution of HiRISE do not erode into the scree slope they are flowing on. RSL also incrementally lengthen compared to SS, which rarely ever overprint.

We hypothesize that SS are indeed dusty avalanches that are capable of being triggered on below the static angle of repose slopes by an energetic trigger. SS flows follow topographic profiles and flow on low-angle slopes. They must possess low friction with the surrounding slope, possibly caused by triboelectric charging of the dust. The timing of SS likely occurs when cameras are inactive, as direct observations of SS in progress (no evidence of incrementally lengthening that cannot be explained by overprinting) or associated dust clouds have not been captured, unlike dust devils or debris flows off the northern polar layered deposits.

RSL are found in regions with low albedo, suggesting a lower amount of dust covering the surface. We hypothesize that RSL are granular flows containing minimal dust content, resulting in higher friction with the scree slope, causing RSL to stop on angle-of-repose slopes. However, RSL exhibit continuous resetting and incremental lengthening over hundreds of sols. We hypothesize that RSL are formed by numerous granular flows comprising of fine- to coarse-grained sediment. Their darker color arises from their lower dust content compared to the surrounding slopes. Moreover, their albedo quickly reset in less than a MY, as only a minimal dust accumulation is required to fade them to match with their low-albedo surroundings.

6. Conclusions

Our comprehensive mapping effort over 32 CTX images revealed a total of 702 slope streaks, the cast majority of which were concentrated in the middle OMA unit. This prevalence is likely attributed to several factors, including the larger scree slopes and the presence of more continuous and higher elevation ridges within the middle OMA unit compared to the lower OMA

unit (**Fig. 2; Table 2**). Within the middle OMA, the majority of SS displayed a SE-facing orientation, with a significantly smaller population forming in a NW-facing direction on the other side of the parallel ridges (**Fig. 3**). This observation underscores the significance of geomorphological characteristics and subtle variations in local topography and microclimatic conditions can lead to optimal conditions for SS formation.

When comparing SS to RSL, distinct differences in their starting and stopping slope angles become apparent. Our observations reveal that the starting slopes of SS are significantly shallower than those of RSL (**Fig. 4**). Only ~2.5% of SS starting angles are above the assumed static angle of repose, in contrast to RSL where the median is near the static angle of repose (**Fig. 4**), implying an undetected energetic triggering mechanism for SS. We propose that surficial wind interactions with the surface or a Knudsen pump phenomenon could serve as potential triggers for SS. It is likely that SS flows are composed of a significant portion of dust. As the flow progresses downhill, this dust becomes airborne, dispersing into local and regional atmospheric circulations at the conclusion of the SS flow event. This could explain why no terminal deposits have been observed. Furthermore, the stopping slopes of SS (median of ~16°) suggest continued flows down slopes well below the dynamic angle of repose (**Fig. 4**). This indicates that SS must possess low friction with the surrounding slope, possibly facilitated by triboelectric charging of the dust. This charging phenomenon could reduce friction and enable the downward movement of the granular material comprising SS. In contrast, we hypothesize that RSL are numerous granular flows containing minimal dust content. Consequently, these flows exhibit higher friction with the scree slope, causing them to come to a halt on angle-of-repose slopes. RSL likely fade faster than SS due to the surrounding slopes in RSL regions having significantly less dust cover. Additionally, RSL flows are significantly smaller, thereby reducing the amount of darkening due to roughness.

We also observe a notable six-fold increase in SS formation enhancement in SS formation near the equinoxes compared to the solstices (**Fig. 8**). Additionally, the long-term SS formation rate varies by a factor of at least two (**Fig. 12a**), with an apparent enhancement in SS formation immediately after PEDEs and a diminished rate three Mars years after a PEDE. This suggests that the remobilization of the dust immediately after a PEDE enhances SS activity. Similarly, mineralogy suggests that the only change between the material inside and outside of a slope streak is a reduction of relatively-fresh dust within the streak (**Fig. 16**). Consequently, fading is

primarily attributed to dust accumulation and dust transport, which smooths out mm- to cm-scale surface roughness caused by SS flows.

Our site exhibits the greatest SS formation rate and fastest fading rate yet quantified. The correlation between SS formation and fading (**Fig. 8**), suggests that dust accumulation plays a pivotal role in SS formation dynamics. The topography of our survey site appears uniquely suited for SS formation. The elevated northern ridges likely influence the nighttime low-level jet to remain at higher altitudes over the southern portions of the study site, facilitating increased dust deposition (**Figs. 17**-**21**).

Throughout much of the year, strong daytime winds blow towards the SE, albeit with moderation around L_s 280°, coinciding with minimal SS activity (**Fig. 19**). These winds, in concert with the surface interactions, or possibly in conjunction with vortices or a Knudsen pump phenomenon, likely act as triggers for the formation of SS on slopes mantled with relatively-fresh dust. We propose that the presence of relatively-fresh dust is essential for enhancing wind-surface interactions, potentially through the formation of dust aggregates (**Fig. 22b**).

In summary, our findings support an energetic-triggered dry avalanche hypothesis of SS formation that is recharged due to dust accumulation and transport. The absence of SS formation around the L_s 90° solstice season can be attributed to the scarcity of fresh dust in the Martian atmosphere during that season. Conversely, the L_s 270° solstice season lacks strong daytime winds, diminishing the effect of a Knudsen pump phenomenon, coupled with reduced insolation, further reducing SS formation potential.

Lastly, we recommend the use of CTX multi-temporal imaging for monitoring SS, given its wide field of view, adequate resolution, and dynamic range. Regular acquisition of 4 to 6 CTX images at multiple SS monitoring sites would greatly enhance our ability to study SS formation and fading mechanism, allowing us to further test the hypothesis put forward in this research.

Acknowledgments. The authors thank reviewer Mikhail Kreslavsky whose suggestions significantly increased the scientific merit of the paper. The authors further thank reviewer Mikhail Kreslavsky and the anonymous reviewer for their detailed comments on the manuscript. D.S., R.H, T.M., H.K, and K.P. were supported by NASA grant #80NSSC20K1412. The authors thank Robert Grimm for intellectual discussions regarding this subject. This research has made

use of the USGS Integrated Software for Imagers and Spectrometers (ISIS) and Java Mission-planning and Analysis for Remote Sensing (JMARS).

Appendix A. Supplementary data can be download (link to be provided by publisher)

Data Availability. CTX data are available on the NASA Planetary Data System (https://pds.nasa.gov). Image IDs are included in the main body of the text. Data for this paper can be found in *Stillman* (2024).

References

Acton, C.H., 1996, Ancillary data services of NASA's Navigation and Ancillary Information Facility, *Planetary and Space Science*, 44, 65-70. DOI 10.1016/0032-0633(95)00107-7

Aharonson, O., N. Schorghofer, and M. F. Gerstell, 2003, Slope streak formation and dust deposition rates on Mars. *J. Geophys. Res.*, 108(E12), 5138, doi:10.1029/2003JE002123

Atwood-Stone, C., McEwen, A.S., 2013. Avalanche slope angles in low-gravity environments from active Martian sand dunes, *Geophys. Res. Lett.* 40, 2929–2934. doi:10.1002/grl.50586

Baratoux, D., Mangold, N., Forget, F., Cord, A., Pinet, P., Daydou, Y., Jehl, A., Masson, P., Neukum, G., & The HRSC CO-Investigator Team, 2006. The role of the windtransported dust in slope streaks activity: evidence from the HRSC data. *Icarus* 183, 30–45. doi:10.1016/j.icarus.2006.01.023

Bell et al., 2013. *International Journal of Mars Science and Exploration*, 8, p. 1-14

Bergonio, J.R., K.M. Rottas, N. Schorghofer, 2013. Properties of martian slope streak populations. *Icarus*, 225, 194-199.

Beyer, R.A., O. Alexandrov, and S. McMichael, 2018. The Ames Stereo Pipeline: NASA's Open Source Software for Deriving and Processing Terrain Data, *Earth and Space Science*, 5, 537-548. https://doi.org/10.1029/2018EA000409.

Bhardwaj, A., Sam, L., Martín-torres, F.J., Zorzano, M., Fonseca, R.M., 2017. Martian slope streaks as plausible indicators of transient water activity. *Sci. Rep*. 1–14. doi:10.1038/s41598-017-07453-9

Bhardwaj, A., Sam, L., Martín-torres, F.J., Zorzano, M.-P., 2019. Are Slope Streaks Indicative of Global-Scale Aqueous Processes on Contemporary Mars?, *Rev. Geophys*. 57, 1–30. doi:10.1029/2018RG000617

Boynton, W. V. et al., 2007. Concentration of H, Si, Cl, K, Fe, and Th in the low-and mid-latitude regions of Mars. *J. Geophys. Res-Planet 112(E12)*, doi:10.1029/2007JE002887.

Bridges, N.T. et al., 2010. Aeolian bedforms, yardangs, and indurated surfaces in the Tharsis Montes as seen by the HiRISE Camera: Evidence for dust aggregates, Icarus, 205, 165-182.

Brusnikin, E.S., et al., 2016. Topographic measurements of slope streaks on Mars. *Icarus* 278, 52–61. doi:10.1016/j.icarus.2016.06.005

Burleigh KJ, Melosh HJ, Tornabene LL, et al. 2012, Impact Airblast Triggers Dust Avalanches on Mars. *Icarus* 217), 194–201; doi: 10.1016/j.icarus.2011.10.026.

Carrozzo, F.G, G. Bellucci, F. Altieri, E.D'Aversa, J.-P. Bibring, 2009, Mapping of water frost

and ice at low latitudes on Mars, *Icarus, 203*, 406-420.
Charalambous, C., McClean, J.B., Baker, M., Pike, W.T., Golombek, M., Lemmon, M., Ansan, V., Perrin, C., Spiga, A., Lorenz, R.D., Banks, M.E., Murdoch, N., Rodriguez, S., Weitz, C.M., Grant, J.A., Warner, N.H., Garvin, J., Daubar, I.J., Hauber, E., Stott, A.E., Johnson, C.L., Mittelholz, A., Warren, T., Navarro, S., Sotomayor, L.M., Maki, J., Lucas, A., Banfield, D., Newman, C., Viúdez-Moreiras, D., Pla-García, J., Lognonné, P., Banerdt, W.B., 2021. Vortex-Dominated Aeolian Activity at InSight's Landing Site, Part 1: Multi-Instrument Observations, Analysis, and Implications. *J. Geophys. Res. Planets 126*, 1–51. https://doi.org/10.1029/2020JE006757
Christensen, P. R., Engle, E., Anwar, S., Dickenshied, S., Noss, D., Gorelick, N., et al., 2009. JMARS - A Planetary GIS, *American geophysical union fall meeting*, San Francisco, CA, December 14–December 18, 2009, [abstract].
Chuang, F.C., et al., 2007. HiRISE observations of slope streaks on Mars, *Geophys. Res. Lett*. 34, 6–11. doi:10.1029/2007GL031111
Chuang, F.C., Beyer, R.A., Bridges, N.T., 2010. Modification of martian slope streaks by eolian processes, *Icarus* 205, 154–164. doi:10.1016/j.icarus.2009.07.035
Dundas, C.M. et al., 2017. Granular flows at recurring slope lineae on Mars indicate a limited role for liquid water, *Nature Geoscience*, 10, 903-907.
Dundas, C.M., 2020. Geomorphological evidence for a dry dust avalanche origin of slope streaks on Mars, *Nature Geoscience*, 13, 473-476.
Ermakov, A.I., Kreslavsky, M.A., Scully, J.E.C., Hughson, K.H.G., Park, R.S., 2019, Surface Roughness and Gravitational Slope Distributions of Vesta and Ceres, *J. Geophys. Res. Planets* 124, 14–30. doi:10.1029/2018JE005813
Ewing, R.C., Lapotre, M.G.A., Lewis, K.W., Day, M., Stein, N., Rubin, D.M., Sullivan, R., Banham, S., Lamb, M.P., Bridges, N.T., Gupta, S., Fischer, W.W., 2017. Sedimentary processes of the Bagnold Dunes: Implications for the eolian rock record of Mars, *J. Geophys. Res. Planets* 122, 2544–2573. doi:10.1002/2017JE005324
Ferris, J.C., 2002. Dark slope streaks on Mars: are aqueous processes involved? *Geophys. Res. Lett*. 29, 5–8. doi:10.1029/2002GL014936
Fischer, E., G. M. Martínez, H. M. Elliott, and N. O. Rennó, 2014. Experimental evidence for the formation of liquid saline water on Mars. *Geophys. Res. Lett.*, 41, doi:10.1002/2014GL060302.
Forget, F. et al., 1999. Improved general circulation models of the Martian atmosphere from the surface to above 80 km, *J. Geophys. Res.*, 104, 24155-24176.
Fergason, R. L, Hare, T. M., & Laura, J., 2018, Mars MGS MOLA - MEX HRSC Blended DEM Global 200m v2, Astrogeology PDS Annex, U.S. Geological Survey, http://bit.ly/HRSC_MOLA_Blend_v0.
Ferguson, H. M., and B. K. Lucchitta, 1984, Reports of the Planetary Geology Program 1983, NASA Tech. Memo., TM-86246, 188-190.
Goetz, W., Pike, W.T., Hviid, S.F., Madsen, M.B., Morris, R. V, Hecht, M.H., Staufer, U., Leer, K., Sykulska, H., Hemmig, E., Marshall, J., Morookian, J.M., Parrat, D., Vijendran, S., Bos, B.J., El Maarry, M.R., Keller, H.U., Kramm, R., Markiewicz, W.J., Drube, L., Blaney, D., Arvidson, R.E., Bell, J.F., Reynolds, R., Smith, P.H., Woida, P., Woida, R., Tanner, R., 2010. Microscopy analysis of soils at the Phoenix landing site, Mars: Classification of soil particles and description of their optical and magnetic properties. *J. Geophys. Res. 115*, E00E22. https://doi.org/10.1029/2009JE003437

Gough, R. V. et al., 2017. Brine formation via deliquescence by salts found near Don Juan Pond, Antarctica: Laboratory experiments and field observational results. *Earth & Planetary Science Letters*, 476, 189-198.

Gough, R. V. et al., 2020. Changes in Soil Cohesion Due to Water Vapor Exchange: A Proposed Dry-Flow Trigger Mechanism for Recurring Slope Lineae on Mars, *Geophys. Res. Lett*, 47, e2020GL087618. https://doi.org/10.1029/2020GL087618

Greeley, R., 1979. Silt-clay aggregates on Mars. *J. Geophys. Res. Solid Earth 84*, 6248–6254. https://doi.org/10.1029/jb084ib11p06248

Haberle, R. M. et al., 2019, Documentation of the NASA/Ames Legacy Mars Global Climate Model: Simulations of the present seasonal water cycle, *Icarus*, 333, 130-164, doi:10.1016/j.icarus.2019.03.026

Hecht, M.H. et al., 2009. Detection of Perchlorate and the Soluble Chemistry of Martian Soil at the Phoenix Lander Site, *Science*, 325, 64-67.

Herkenhoff, K.E., Squyres, S.W., Anderson, R., Archinal, B.A., Arvidson, R.E., Barrett, J.M., Becker, K.J., Bell, J.F.I., Budney, C., Cabrol, N.A., Chapman, M.G., Cook, D., Ehlmann, B.L., Farmer, J., Franklin, B., Gaddis, L.R., Galuszka, D.M., Garcia, P.A., Hare, T.M., Howington-Kraus, E., Johnson, J.R., Johnson, S., Kinch, K., Kirk, R.L., Lee, E.M., Leff, C., Lemmon, M., Madsen, M.B., Maki, J.N., Mullins, K.F., Redding, B.L., Richter, L., Rosiek, M.R., Sims, M.H., Soderblom, L.A., Spanovich, N., Springer, R., Sucharski, R.M., Sucharski, T., Sullivan, R., Torson, J.M., Yen, A., 2006. Overview of the Microscopic Imager Investigation during Spirit's first 450 sols in Gusev crater. *J. Geophys. Res. 111*, E02S04. https://doi.org/10.1029/2005JE002574

Heyer, T., Kreslavsky, M., Hiesinger, H., Reiss, D., Bernhardt, H., Jaumann, R., 2019. Seasonal formation rates of martian slope streaks. *Icarus*323, 76–86. https://doi.org/10.1016/j.icarus.2019.01.010.

Heyer T., et al., 2020. Dust devil triggering of slope streaks on Mars. *Icarus*, 351, 113951.

I-MIM MDT (2022) Final Report of the International Mars Ice Mapper Reconnaissance/Science Measurement Definition Team. 239 pp., posted online at https://science.nasa.gov/researchers/ice-mapper-measurement-definition-team.

Kaplan H. H., D. E. Stillman, R. Hoover, T. Michaels, L. Fenton, K.M. Primm, 2023, Visible and Near-Infrared Spectral Properties of Martian Slope Streaks, Planetary Science Journal 4:232, https://doi.org/10.3847/PSJ/ad037e.

King, C., N. Schorghofer, K. Wagstaff, 2010, Martian slope streaks form sporadically throughout the year. Lunar and Planetary Institute Science Conference Abstracts, vol. 41, p. 1542

Kreslavsky, M.A., Head, J.W., 2009. Slope streaks on Mars: a new "wet" mechanism. *Icarus* 201, 517–527. doi:10.1016/j.icarus.2009.01.026

Kreslavsky, M. & Head, J. (2019) Slope Streaks on Mars: Synthesis and a New Proposed Formation Mechanism, 9th Int. Mars Conf., #6245, https://www.hou.usra.edu/meetings/ninthmars2019/pdf/6245.pdf

Lange, L., Piqueux, S., & Edwards, C. S. (2022). Gardening of the Martian regolith by diurnal CO_2 frost and the formation of slope streaks. *Journal of Geophysical Research: Planets, 127*, e2021JE006988. https://doi.org/10.1029/2021JE006988

Levy, J.S., et al., 2011, Water tracks and permafrost in Taylor Valley, Antarctica: Extensive and shallow groundwater connectivity in a cold desert ecosystem. *GSA Bulletin*, 123, 2295-2311.

Malin, M.C., and K.S. Edgett, 2001, Mars global surveyor Mars orbiter camera: interplanetary cruise through primary mission. *Journal of Geophysical Research: Planets*, 106, 23429-23570.

Malin, M.C., et al., 2007, Context Camera Investigation on board the Mars Reconnaissance Orbiter. *J. Geophys. Res. Planets*, 112, E05S04.

Martínez, G.M., et al., 2017, *Space Sci. Rev*., The Modern Near-Surface Martian Climate: A Review of In-situ Meteorological Data from Viking to Curiosity, 212, 295-338.

McEwen, A.S., et al., 2007, Mars reconnaissance orbiter's high resolution imaging science experiment (HiRISE). *Journal of Geophysical Research: Planets*, 112. E05S02. doi:10.1029/2005JE002605

McEwen, A.S., et al., 2011, Mars reconnaissance orbiter's high resolution imaging science experiment (HiRISE). *Science*, 333, 740-743.

McEwen, A.S., et al., 2021, Mars: Abundant Recurring Slope Lineae (RSL) Following the Planet-Encircling Dust Event (PEDE) of 2018, *J. Geophys. Res. Planets*, 126, e2020JE006575.

Merrison, J., Jensen, J., Kinch, K., Mugford, R., Nørnberg, P., 2004. The electrical properties of Mars analogue dust. *Planet. Space Sci. 52*, 279–290. https://doi.org/10.1016/j.pss.2003.11.003

Merrison, J.P., Gunnlaugsson, H.P., Nørnberg, P., Jensen, A.E., Rasmussen, K.R., 2007. Determination of the wind induced detachment threshold for granular material on Mars using wind tunnel simulations. *Icarus 191*, 568–580. https://doi.org/10.1016/j.icarus.2007.04.035

Millour, E., et al., 2015, The Mars Climate Database (MCD version 5.2). In Eur. Planet. Sci. Cong. EPSC2015-438 Nantes, France.

Miyamoto, H., Dohm, J.M., Beyer, R.A., Baker, V.R. (2004) Fluid dynamical implications of anastomosing slope streaks on Mars. *J. Geophys. Res. Planets, 109*. https://doi.org/10.1029/2003JE002234

Montabone, L., et al., 2015, Eight-year climatology of dust optical depth on Mars, *Icarus*, 251, 65-95.

Moore, H.J., Jakosky, B.M., 1989. Viking landing sites, remote-sensing observations, and physical properties of Martian surface materials. *Icarus 81*, 164–184. https://doi.org/10.1016/0019-1035(89)90132-2

Morris, E.C., 1982, Aureole deposits of the Martian volcano Olympus Mons. *J. Geophys. Res.*, 87, 1164-1178.

Morris, E.C., and K.L. Tanaka, 1994, Geologic maps of the Olympus Mons region of Mars, U.S. Geol. Surv. Misc. Invest. Ser., Map I-2327-B. doi: 10.3133/i2327

Murchie, S., et al., 2007, Compact Reconnaissance Imaging Spectrometer for Mars (CRISM) on Mars ReconnaissanceOrbiter (MRO),J. Geophys. Res., 112, E05S03.

Mushkin, A., Gillespie, A.R., Montgomery, D.R., Schreiber, B.C., Arvidson, R.E., 2010. Spectral constraints on the composition of low-albedo slope streaks in the Olympus Mons Aureole. *Geophys. Res. Lett.* 37, 1–5. doi:10.1029/2010GL044535

Mustard, J.F., et al., 2008, Hydrated silicate minerals on Mars observed by the Mars Reconnaissance Orbiter CRISM instrument, *Nature*, 454, 305-309.

Phillips, C.B., Burr, D.M., Beyer, R.A., 2007. Mass movement within a slope streak on Mars. *Geophys. Res. Lett.* 34, 1–5. doi:10.1029/2007GL031577

Piqueux, S., Kleinbohl, A., Hayne, P. O., Heavens, N. G., Kass, D. M., McCleese, D. J., Schofield, J. T., Shirley, J. H., 2016. Discovery of a widespread low-latitude diurnal CO2

frost cycle on Mars. *J. Geophys. Res.* 121, 1174-1189, https://doi.org/10.1002/2016JE005034
Rafkin, S. C. et al., 2001, The Mars Regional Atmospheric Modeling System: Model Description and Selected Simulations, *Icarus*, 151, 228–256.
Rafkin, S.C. and T.I. Michaels, 2019, The Mars Regional Atmospheric Modeling System (MRAMS): Current Status and Future Directions, *Atmosphere*, 10, 747, doi:10.3390/atmos10120747
Schaefer, E.I., McEwen, A.S., Sutton, S.S., 2019. A case study of recurring slope lineae (RSL) at Tivat crater: Implications for RSL origins. *Icarus* 317, 621–648. doi:10.1016/j.icarus.2018.07.014
Schmidt, F., Andrieu, F., Costard, F., Kocifaj, M., Meresescu, A.G., 2017. Formation of recurring slope lineae on Mars by rarefied gas-triggered granular flows. *Nat. Geosci.* 10, 270–273. doi:10.1038/ngeo2917
Schorghofer, N., and King, 2011, Sporadic formation of slope streaks on Mars. *Icarus*, 216, 159-168.
Schorghofer, N., et al., 2002, Slope streaks on Mars: Correlations with surface properties and the potential role of water. *Geophys. Res. Lett*., 29, 2126.
Schorghofer, N., et al., 2007, Three decades of slope streak activity on Mars. *Icarus*, 191, 132-140.
Shao, Y., 2008. Physics and Modelling of Wind Erosion. Springer Dordrecht. https://doi.org/10.1007/978-1-4020-8895-7
Stillman, D.E., 2018. Unraveling the Mysteries of Recurring Slope Lineae, Dynamic Mars, 51-85.
Stillman, D. (2024) Comprehensive Observations and Geostatistics of Slope Streaks within the Olympus Mons Aureole (Version 1) [Dataset], Zenodo. https://doi.org/10.5281/zenodo.10735886
Stillman, D.E., and R.E. Grimm, 2018, Two pulses of seasonal activity in martian southern mid-latitude recurring slope lineae (RSL), *Icarus*, 302, 126-133.
Stillman, D.E., et al., 2014, New observations of martian southern mid-latitude recurring slope lineae (RSL) imply formation by freshwater subsurface flows, *Icarus*, 233, 328-341.
Stillman, D.E., et al., 2020, Evaluation of wet and dry recurring slope lineae (RSL) formation mechanisms based on quantitative mapping of RSL in Garni Crater, Valles Marineris, Mars, *Icarus* 335, 113420.
Sullivan, R., Thomas, P., Veverka, J., Malin, M., Edgett, K.S., 2001. Mass movement slope streaks imaged by the Mars Orbiter Camera. *J. Geophys. Res. E Planets* 106, 23607–23633. doi:10.1029/2000JE001296
Sullivan, R., Arvidson, R., Bell, J.F., Gellert, R., Golombek, M., Greeley, R., Herkenhoff, K., Johnson, J., Thompson, S., Whelley, P., Wray, J., 2008. Wind-driven particle mobility on Mars: Insights from Mars Exploration Rover observations at "El Dorado" and surroundings at Gusev Crater. *J. Geophys. Res. 113*, E06S07. https://doi.org/10.1029/2008JE003101
Tanaka et al., 2014, Geologic map of Mars, U.S. Geological Survey Scientific Investigations Map 3292, 43 p., https://dx.doi.org/10.3133/sim3292.
Wang, A et al., 2019. Subsurface Cl-bearing salts as potential contributors to recurring slope lineae (RSL) on Mars, *Icarus*, 333, 464-480.
Valantinas, A., Becerra, P., Pommerol, A., et al. 2021, Multi-angular observations of Martian bright slope streaks. *Planetary and Space Science*, 209, 105373
Vaughan, A.F., Johnson, J.R., Herkenhoff, K.E., Sullivan, R., Landis, G.A., Goetz, W., Madsen,

M.B., 2010. Pancam and Microscopic Imager observations of dust on the Spirit Rover: Cleaning events, spectral properties, and aggregates. *Mars J.* 5, 129–145. https://doi.org/10.1555/mars.2010.0005

Vincendon, M., F. Forget, and J. Mustard (2010), Water ice at low to midlatitudes on Mars, *J. Geophys. Res., 115*, E10001, doi:10.1029/2010JE003584.

Vincendon, M., Pilorget, C., Carter, J., Stcherbinine, A., 2019. Observational evidence for a dry dust-wind origin of Mars seasonal dark flows. *Icarus* 325, 115–127. doi:10.1016/j.icarus.2019.02.024

White, B. R., 1979, Soil transport by winds on Mars, *J. Geophys. Res.*, *84*, 4643-4651 https://doi.org/10.1029/JB084iB09p04643.

White, B.R., Lacchia, B.M., Greeley, R., Leach, R.N., 1997. Aeolian behavior of dust in a simulated Martian environment. *J. Geophys. Res. 102*, 25629–25640. https://doi.org/10.1029/97JE01753

Yakovlev, V. (2010) Slope Streaks on Mars — Gravity-Capillary Displays of Water, LPSC 41, #1333, https://www.lpi.usra.edu/meetings/lpsc2010/pdf/1333.pdf

Table 1. The mapped area of NW- and SE-facing slopes range from 15.6 to 29.5°. These slope bounds correspond to the 12.5% and 87.5% percentage values of the starting SS slopes as shown in Fig. 4. Consequently, 75% of the SS should fall within these mapped areas. Note that the mapped NW- and SE-facing slope areas are of comparable size for both the lower and middle OMA units.

Location	Area of NW-facing steep slopes (km^2)	Area of SE-facing steep slopes (km^2)
Lower Unit	31.450	32.971
Middle Unit	78.696	78.213
Study Area	110.146	111.184

Table 2. The data table is organized based on the OMA unit or the summation of units within the study area. Within this framework, the mapped SS are categorized into five distinct groups: (1) originally-mapped SS at MY 28.641 in CTX image P07_003595; (2) originally-mapped SS that faded over the 7.177 MYs between MY 28.641 and MY 35.818 (CTX image N11_066613); (3) new SS that fomred over the 7.177 MYs following MY 28.641; (4) existing SS that were mapped at MY 35.818; (5) total number of unique SS mapped over the 7.177 MYs between MY 28.641 and MY 35.818. Note that the last CTX image acquired (U07_073709) is excluded from this analysis as it only imaged 75% of the study area, which would complicate geostatistical analysis. Furthermore, the SS density (number of SS divided by area) of NW- and SE-facing steep slopes is approximately equal in the lower unit, but heavily skewed toward SE-facing slopes in the middle unit. Additionally, the middle unit exhibits a significantly higher SS rate compared to the lower unit, with the difference being roughly an order of magnitude or more. Moreover, there is variability in the SE/NW ratio of SS rates between MY 28.641 and MY 35.818, with the initial image displaying a greater bias towards SS with SE-facing slopes.

Location	SS Mapped Categories	NW-facing		SE-facing		SE/NW Ratio of SS Rates
		Num	SS Density (km^{-2})	Num	SS Density (km^{-2})	
Lower Unit	Orig. SS at MY 28.641	3	0.095	2	0.061	0.6
	Orig. SS faded over 7.177 MYs	2	0.064	1	0.030	0.5
	New SS over 7.177 MYs	0	0.000	3	0.091	--
	Existing SS at MY 35.818	1	0.032	3	0.091	2.9
	Total Mapped SS	3	0.095	5	0.152	1.6
Middle Unit	Orig. SS at MY 28.641	11	0.140	179	2.289	16.4
	Orig. SS faded over 7.177 MYs	5	0.064	126	1.611	25.4
	New SS over 7.177 MYs	62	0.788	373	4.769	6.1
	Existing SS at MY 35.818	36	0.457	245	3.132	6.8
	Total Mapped SS	73	0.928	552	7.058	7.6
Study Area	Orig. SS at MY 28.641	14	0.127	181	1.628	12.8
	Orig. SS faded over 7.177 MYs	7	0.064	127	1.142	18.0
	New SS over 7.177 MYs	62	0.563	376	3.382	6.0
	Existing SS at MY 35.818	37	0.336	248	2.231	6.6
	Total Mapped SS	76	0.690	557	5.010	7.3

Table 3. The boundaries of each interpreted season alongside their normalized rates and statistical significance. Notably, the normalization and statistical significance, measured by the number of standard deviations between the observed data and the uniform model, highlight the statistically significant seasonality observed during the 90° solstice and 180° equinox seasons. However, further data is required to establish the significance of the other seasons.

Season	Start (sol of the MY)	Stop (sol of the MY)	Start (L_s)	Stop (L_s)	Normalized Rate	Significance (σ)
0° equinox	626	86	337°	42°	1.6±0.5	1.5±1.2
90° solstice	86	290	42°	136°	0.3±0.1	–2.9±0.7
180° equinox	290	448	136°	227°	1.9±0.4	3.5±1.8
270° solstice	448	626	227°	337°	0.6±0.4	–1.7±1.4

Table 4. Modeled estimates of the anticipated number of SS expected to form on the steep slopes of the middle OMA unit throughout a Mars year.

Season	0° Equinox	90° Solstice	180° Equinox	270° Solstice
Sol of the MY	626–86	86–290	290 – 448	448 – 626
L_s Range	337°–42°	42°–136°	136°–227°	227°–337°
NW-facing SS per sol per km^2	2.28E-04	4.28E-05	2.71E-04	7.84E-05
SE-facing SS per sol per km^2	1.74E-03	3.27E-04	2.07E-03	5.99E-04
NW-facing SS estimated in the season over the middle unit	2.3	0.7	3.4	1.1
SE-facing SS estimated in the season over the middle unit	17.7	5.2	25.6	8.3

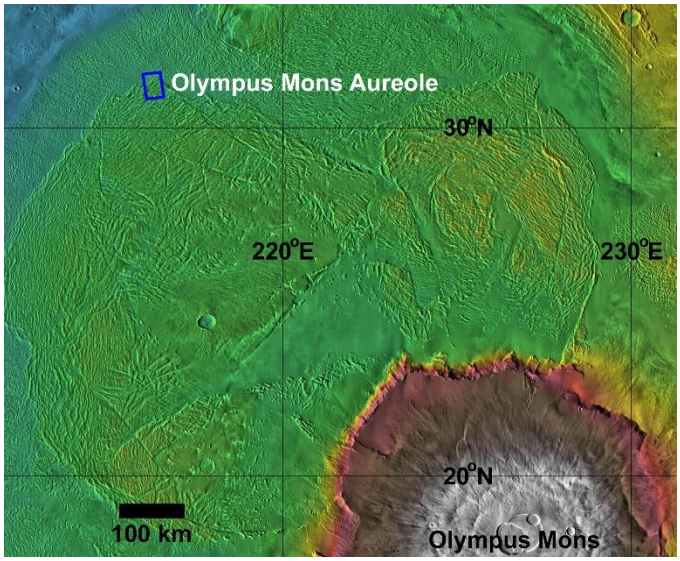

Figure 1. The site (blue rhombus) is situated in close proximity to Olympus Mons. It encompasses both the lower and middle Olympus Mons Aureole (OMA) units, as mapped by *Morris and Tanaka* (1995). The background imagery comprises the THEMIS Daytime IR mosaic, enhanced with colorized with MOLA elevation data (JMARS layer; *Hill et al.*, 2014).

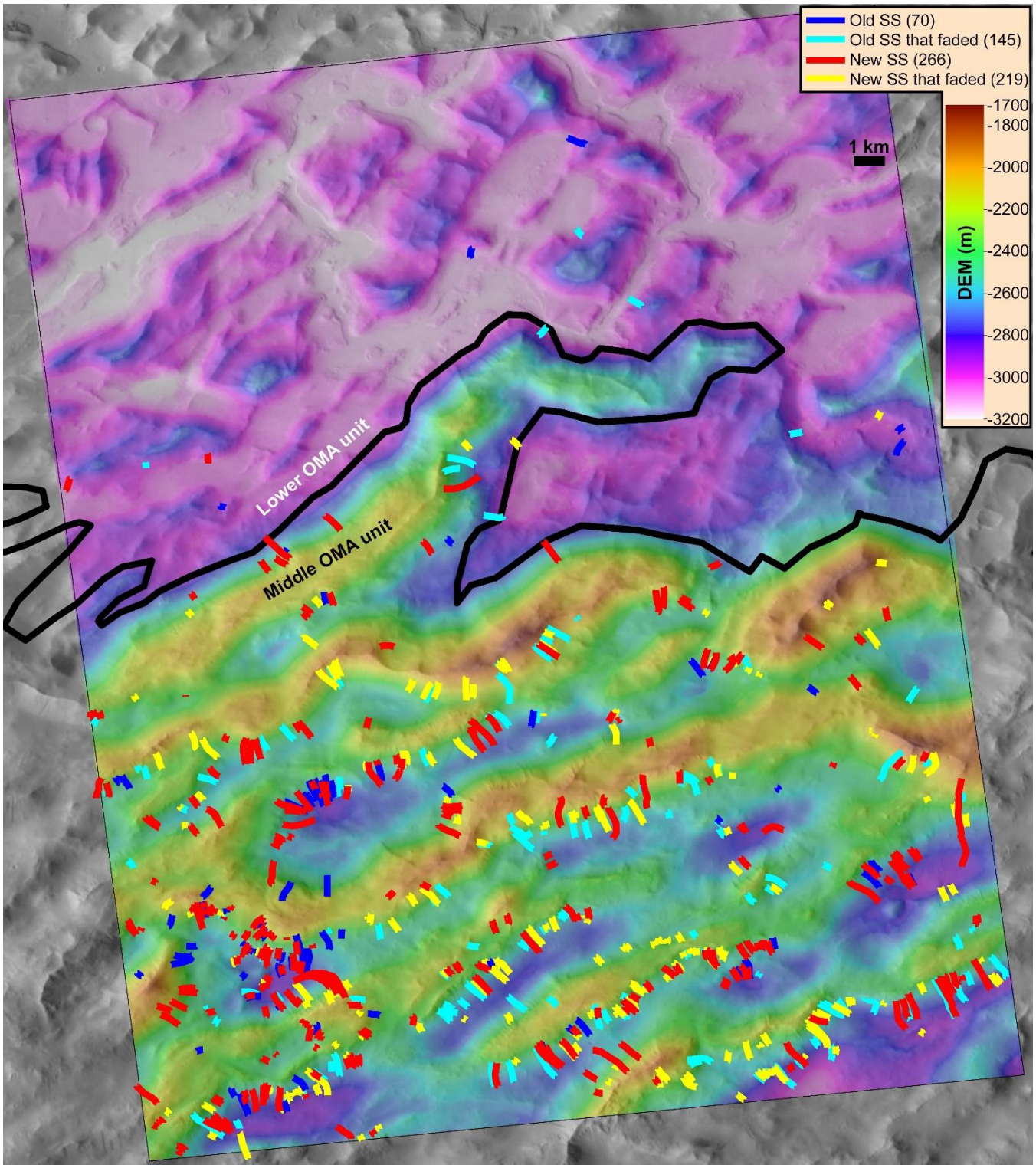

Figure 2. The correlation between SS and geographic features reveal that SS within the OMA exhibit a preference for formation on elevated terrain, particularly in the southern regions of the site. This elevated terrain corresponds to the previously mapped middle OMA unit (*Morris and Tanaka*,1995). Conversely, the northern portion of the site, characterized by lower elevations, corresponds to the lower

OMA unit. The extent of the DEM we constructed and utilized is illustrated by the inset rectangle, color-coded to represent elevation variations.

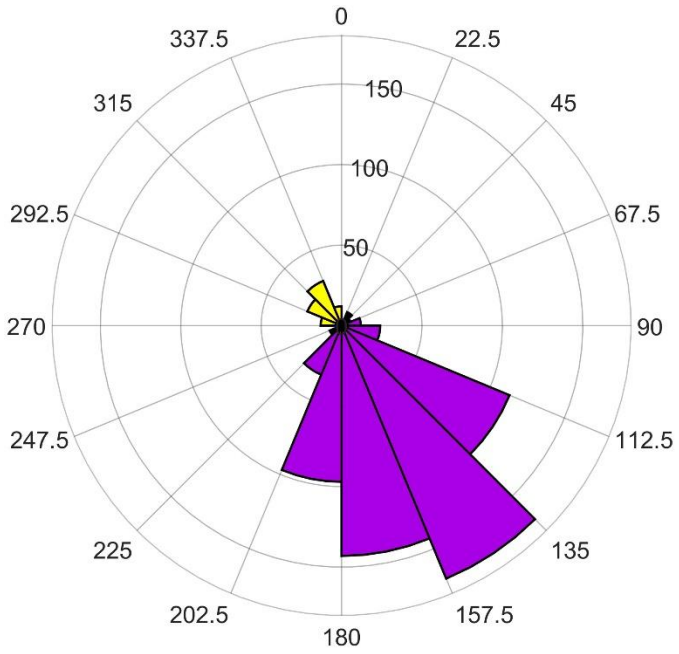

Figure 3. Starting orientation of SS reveal a dominant SE orientation (filled in purple), spanning from 67.5 to 225°. While a minor peak (filled in yellow) is observed from 270-360°, the number of SS associated with this orientation is nearly an order of magnitude lower.

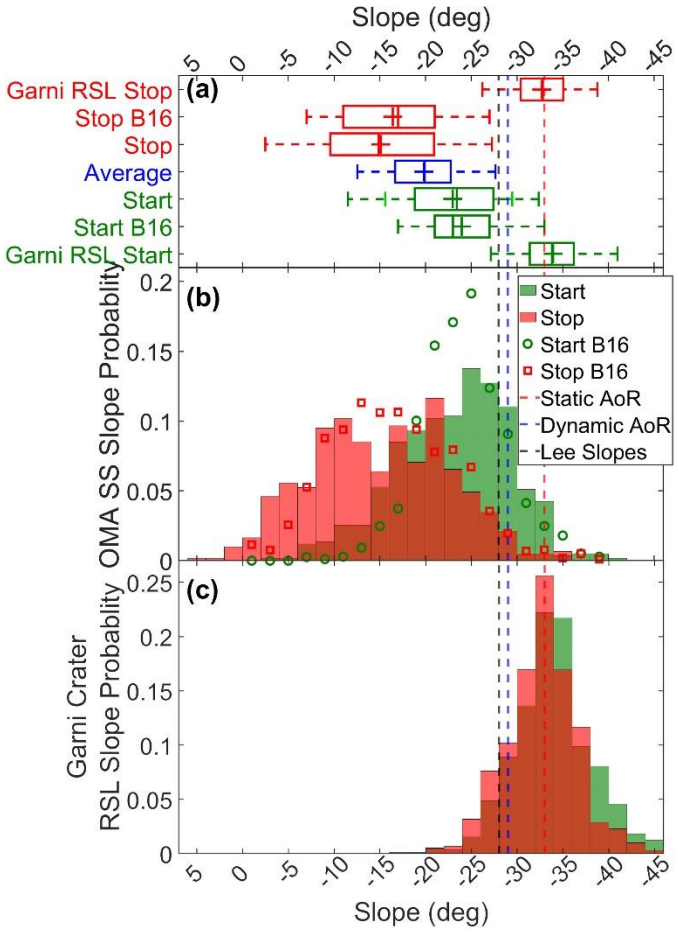

Figure 4. Comparison of the slope distributions of SS mapped at our survey site with those mapped by *Brusnikin et al.* (2016) (B16 in the plot) and RSL distribution (*Stillman et al.,* 2020) is illustrated. Box and whiskers plot **(a)** displays the 5%, 25%, 50%, 75%, and 95% percentiles for slope distributions of the start, entirety, and stop of SS at our survey site, with the mean represented by pluses. Note the whiskers extend to 5 and 95%, except for the light green values, which indicate 12.5 and 87.5% (later utilized in **Table 1 & 2**). **(a and b)** The vertical dashed lines in both **(a)** and **(b)** represent the static angle of repose (AoR; *Ewing et al*., 2017), dynamic angle of repose (*Ewing et al*., 2017), and measured values of lee slopes of martian dunes (*Atwood-Stone and McEwen*, 2013). The histogram in **(b)** displays our SS data compared to *Brusnikin et al.* (2016), showing that our dataset exhibits a broader distribution extending to shallower slopes. Note the *Brusnikin et al.* (2016) dataset was compiled from ~1500 SS from 19 sites, which included our survey site. Additionally, the box plot and whiskers of *Brusnikin et al.* (2016) are approximated since the raw numbers of each SS segment were not published. *Brusnikin et al.* (2016) also indicated maximum slopes >40° at 6 of their 19 sites, hinting at a larger range than observed at our survey site. Note that our starting and stopping slopes have a baseline of 34-42.5 m, as our DEM has a posting every 8.5 m, while *Brusnikin et al.* (2016) calculated their slopes at a 15-30 m baseline. The histogram in **(c)** presents the RSL distribution at Garni Crater reported by *Stillman et al.* (2020), clearly showing that RSL occur on much steeper slopes.

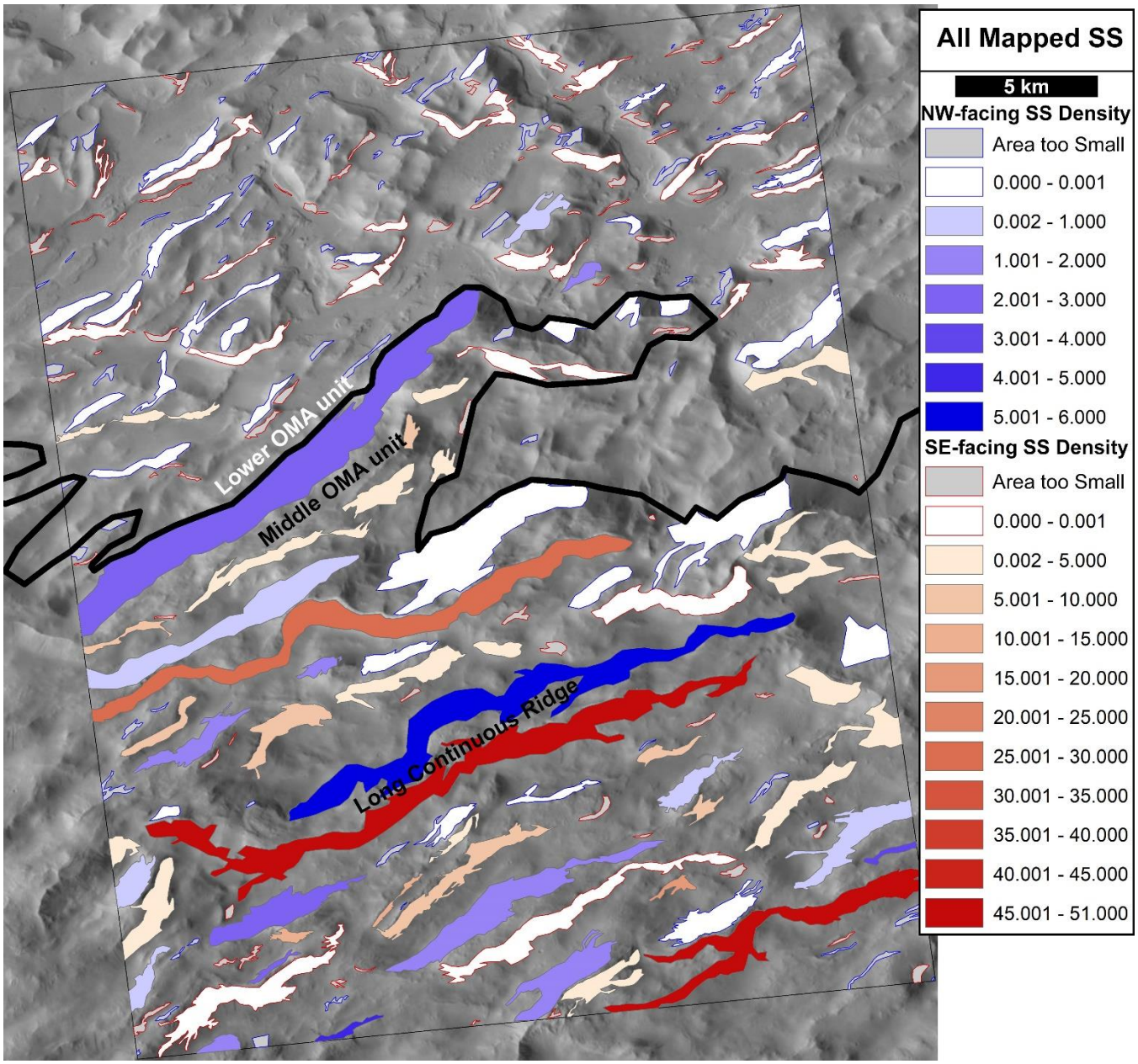

Figure 5. The geographic distribution of SS density among all mapped SS reveals notable patterns. Few SS are observed to form in the lower OMA unit, resulting in a low density in this area. Conversely, both NW- and SE-facing SS exhibit higher densities along lengthy continuous ridges. The highest SE-facing density is observed in the SE corner of the study area, with a density of 50.091 SS per km^2. The inset rectangular outline represents the location of the study area.

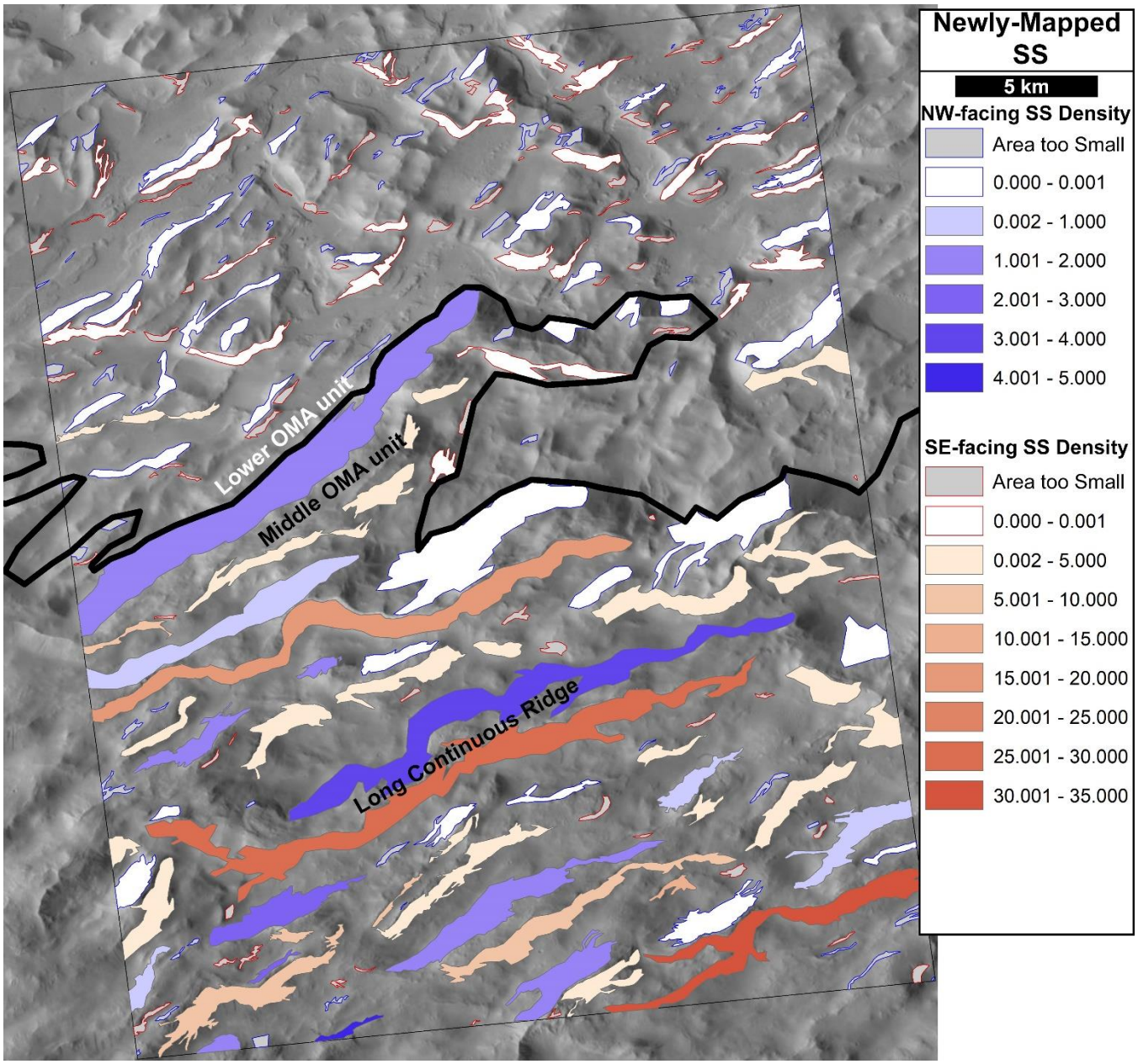

Figure 6. The geographic distribution of SS density for newly-formed SS between MY 28.641 (CTX image: P07_003595) and MY 35.818 (CTX image N11_066613), which span a duration of 7.177 MYs, reveals intriguing patterns. The highest density of newly-formed SS is observed on SE-facing slopes in the southeast region of the study area. Note that the color scales for **Figures 5-7 and S6-S7** remain consistent; however, values exceeding the maximum are masked to ensure clarity.

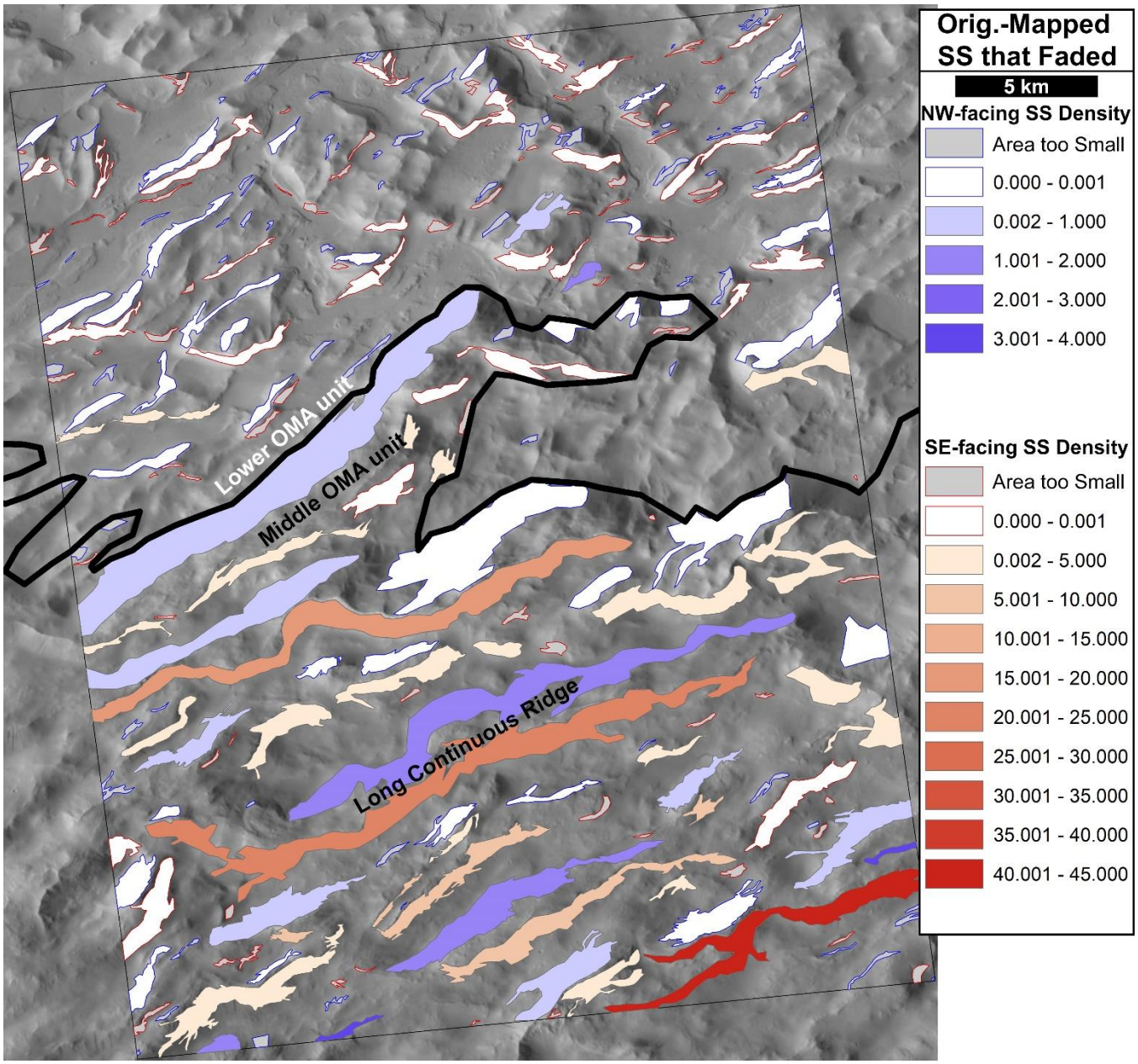

Figure 7. The geographic distribution of SS density for originally-mapped SS at MY 28.641 (CTX image: P07_003595) that faded by MY 35.818 (CTX image N11_066613), which span a duration of 7.177 MYs, reveals intriguing patterns. The highest density of SS fading is observed on SE-facing slopes in the southeastern portion of the study area. Note the color scales for **Figures 5-7 and S6-S7** remain constant; however, values exceeding the maximum are masked to ensure clarity.

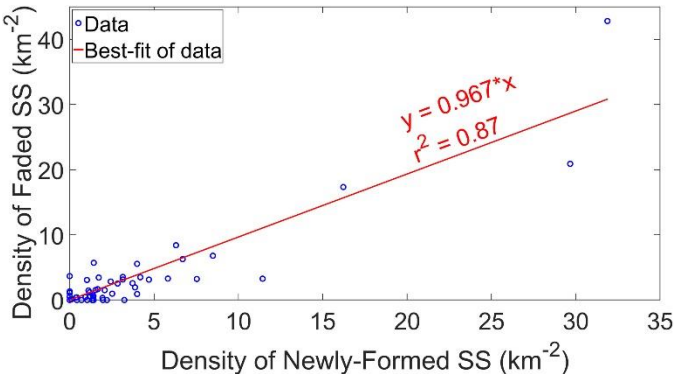

Figure 8. In the cross-plot of the density of newly-formed SS (**Fig. 6**) and originally-mapped SS that faded (**Fig 7**), a notable trend emerges: slopes that exhibit higher rates of SS formation also tend to experience more SS fading. The trendline shows that slopes that form more SS also erase more SS. The linear fit with a slope of ~1 indicates that an equal number of SS form and fade as is expected.

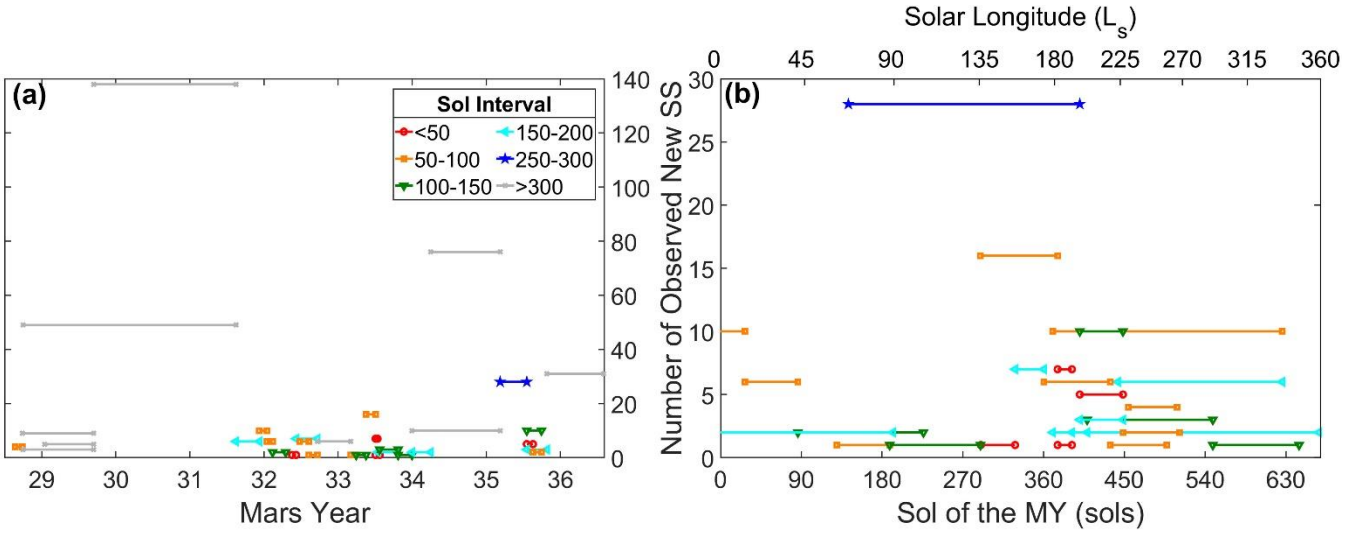

Figure 9. Graphical representation illustrates the variation in the number of newly-observed SS across the CTX pairs, characterized by (**a**) MY and (**b**) sol of the Mars year. Note that no SS were observed in the sol interval of 200-250 sols and sol intervals >300° are omitted in (**b**) for clarity. It is expected that shorter sol intervals would result in fewer newly-formed SS being mapped if SS formation is independent of season.

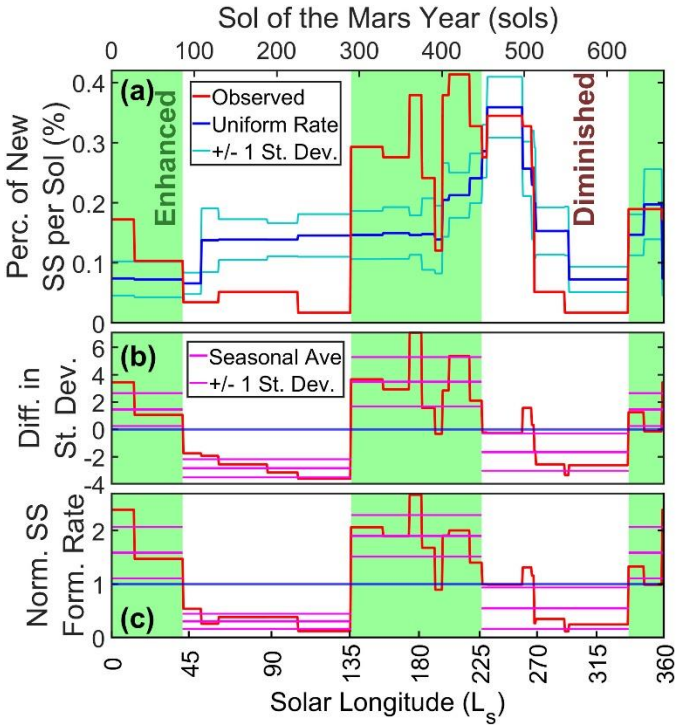

Figure 10. (a) Comparison between the observed data (red) and seasonally uniform model (blue) using a 141-sol interval threshold between CTX image pairs. Error bars representing ±1 standard deviation for the uniform model (cyan) are calculated using the Poisson distribution. Generally, an enhancement or diminishment in seasonality is indicated when the observations exceed or fall below the values predicted by the uniform model, respectively. **(b)** Difference in the number of standard deviations between the observations in **(a)** and the uniform model in **(a)**. **(c)** Plot illustrating normalized SS formation rate as a function of season, with the seasonal rate (thicker magenta line) representing the mean of values associated with each interpreted enhanced or diminished season. Lighter magenta lines depict the ±1 standard deviation variations of the seasonal variation.

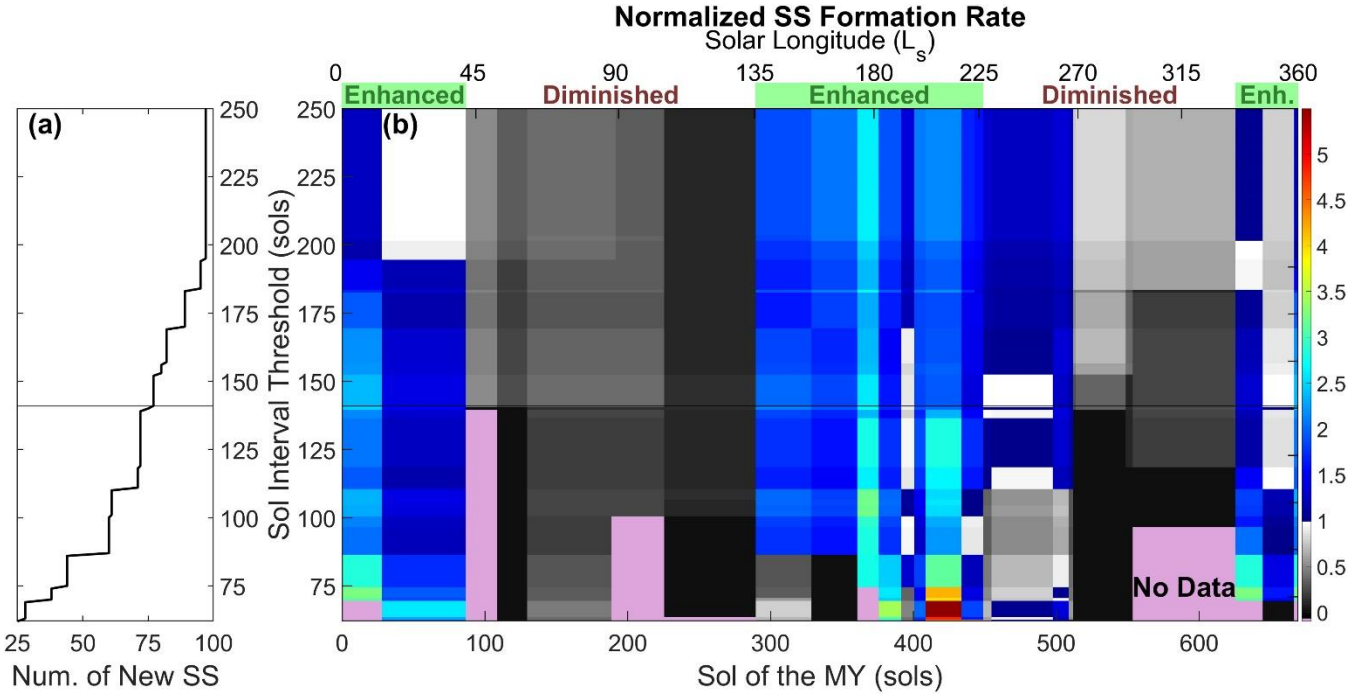

Figure 11. (a) Graph illustrating the total number of newly-mapped SS as a function of the number of sols between the CTX images. (**b**) Filled contours depict the normalized ratio of the observed and uniform rate modeled percentages of newly-mapped SS per sol, as displayed in **Figure 10a**. Colored contours indicate sols where SS formation is enhanced (color scale with positive values), diminished (greyscale with negative values), or where no CTX image pairs are available (pink, representing no data), based on the sol interval threshold. A horizontal line at a sol interval threshold of 141-sols marks the value that was used to interpret the enhanced and diminished zones, as shown in **Fig. 10**. Fig. S9 displays the number of area-normalized CTX images that were used to produce this figure as a function of sol of the MY and sol interval threshold.

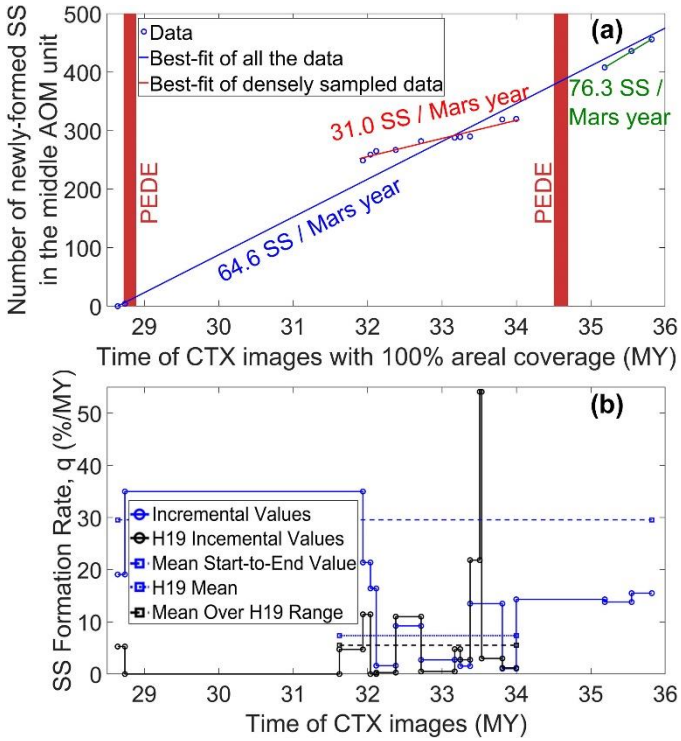

Figure 12. (a) Plot illustrating the formation of newly-formed SS over time, with the slope indicating the rate at which new SS form. Additionally, we highlight instances of Planet-Encircling Dust Events (PEDE). **(b)** Comparison between our observed SS formation rate and the findings of *Heyer et al.* (2019; abbreviated to H19 in legend). Both plots demonstrate that SS formation rates are variable and relatively small during the timeframe examined in the *Heyer et al.* (2019) study.

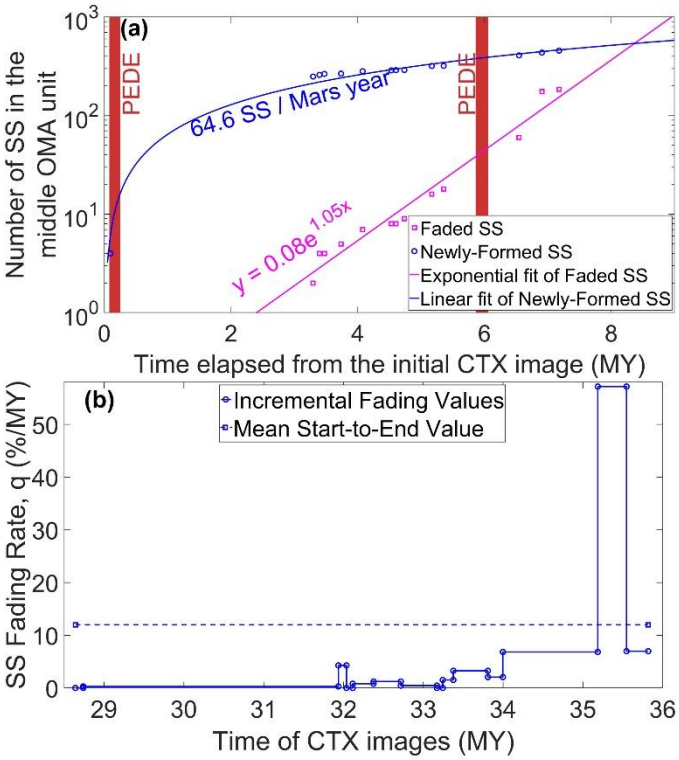

Figure 13. (a) The count of faded SS exhibited an exponential growth pattern from the onset. However, maintaining such a pace would be impractical, as it would surpass the rate of newly-formed SS after ~8.3 MY. **(b)** Incremental and mean fading values were computed following the methodology outlined by *Aharonson et al.* (2003).

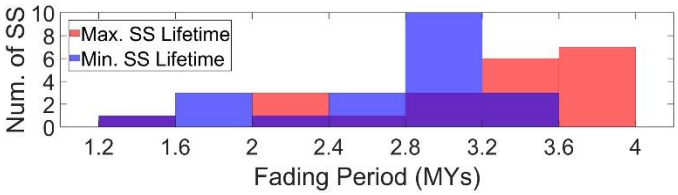

Figure 14. A histogram of 21 slope streaks with their formation and fully-faded dates confined within a range of 144° of L_s. To determine the minimum duration in Mars years between formation and fading, we calculated the difference between the date of the last image in which the SS was not faded and the date of the first image capturing its formation. For the maximum duration, we computed the difference between the date of the image showing the SS fully faded and the date proceeding the one capturing its formation. Overall, our analysis reveals that time-constrained slope streaks tend to fade within ~3 to 3.8 Mars years.

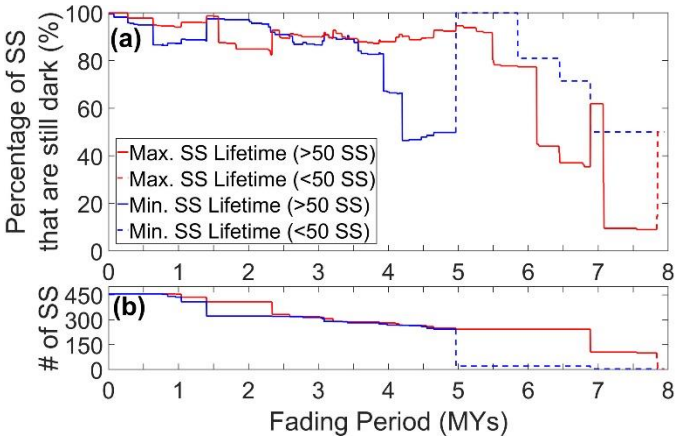

Figure 15. (a) The ratio of newly-formed SS that have not yet faded, relative to the total number of SS plotted against time. **(b)** The number of SS plotted over time. Note that datasets with fewer than 50 SS (dashed lines) exhibit ratios inconsistent with the rest of the data. Maximum and minimum Mars year increments are classified similarly to **Fig. 13**, but these findings are less precise due to uncertainties in the timing of SS formation and fading. Overall, our analysis indicates that 50% of SS fully fade within a timeframe of 4 to 6 Mars years.

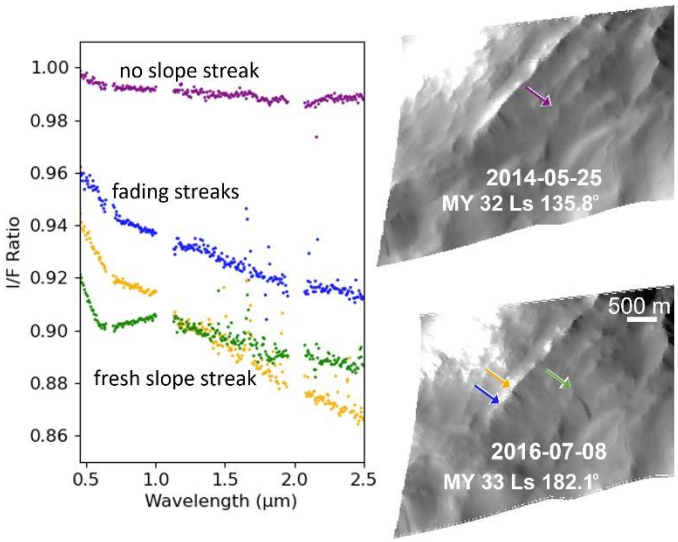

Figure 16. CRISM images acquired in MY 32 (FRS0003005C) and 33 (FRS0003D33A) were examined at our study site. **(a)** Spectral analyses of four slope streaks (averaged across the entire streak and normalized by the adjacent slope to enhance spectral features) and the slope before the formation of a SS are presented. Notably, a correlation exists between lower slope streak albedo and enhanced absorption features near 0.7 μm, a phenomenon observed across various sites and statistically validated (*Kaplan et al.*, 2023). **(b)** CRISM images provide contextual insight into these spectra. Specifically, we show the darkest slope streak formed between MY 32 and 33, and three nearby streaks existed in MY 32 and 33.

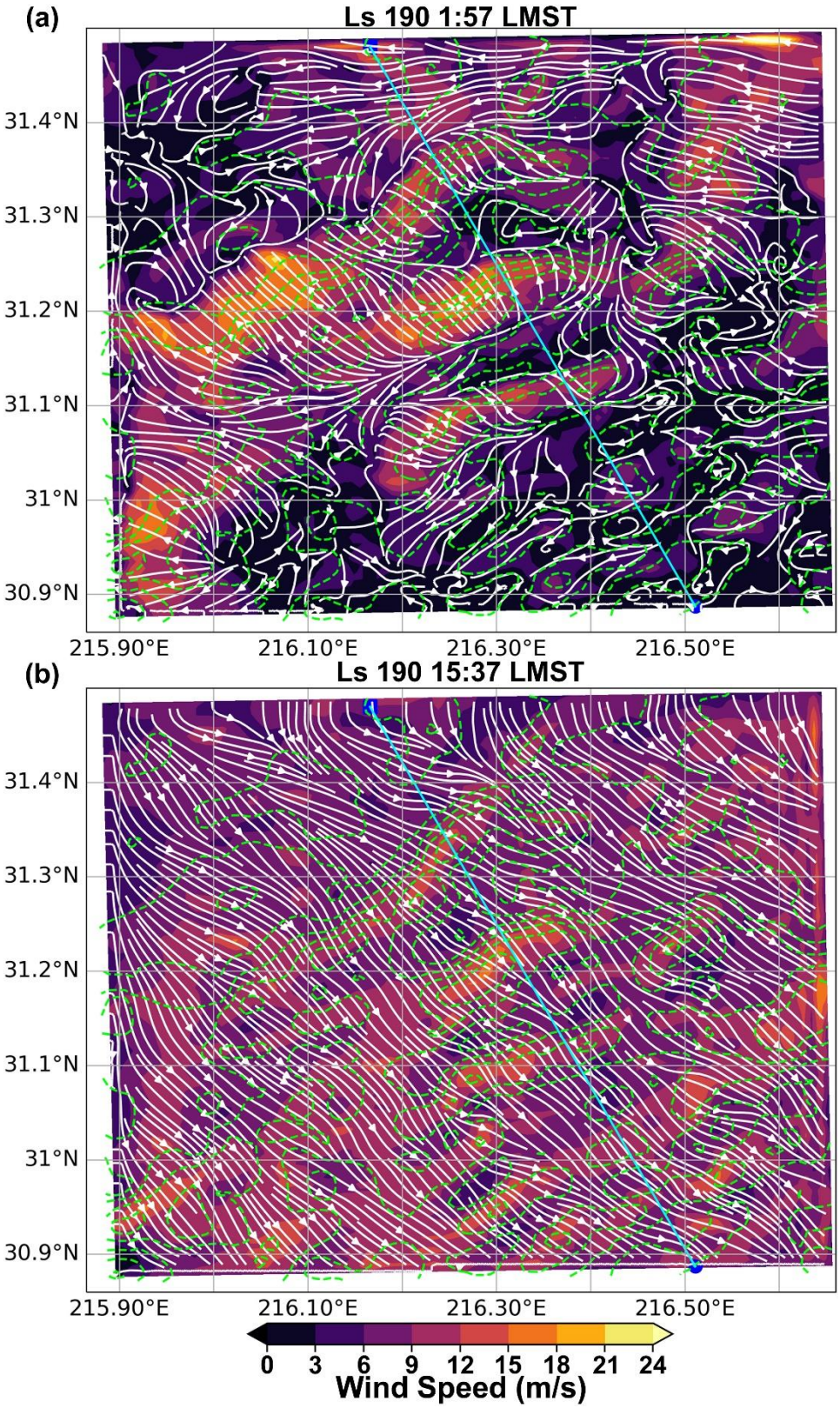

Figure 17. (a) Nighttime and **(b)** daytime surficial wind speed and orientation surrounding the central profile (cyan line) derived from the MRAMS simulation for L_s 190°. Streamline arrows depict wind

orientation, while filled color contours indicate the wind speed. Dashed green contours denote model topography, with LMST representing Local Mean Solar Time.

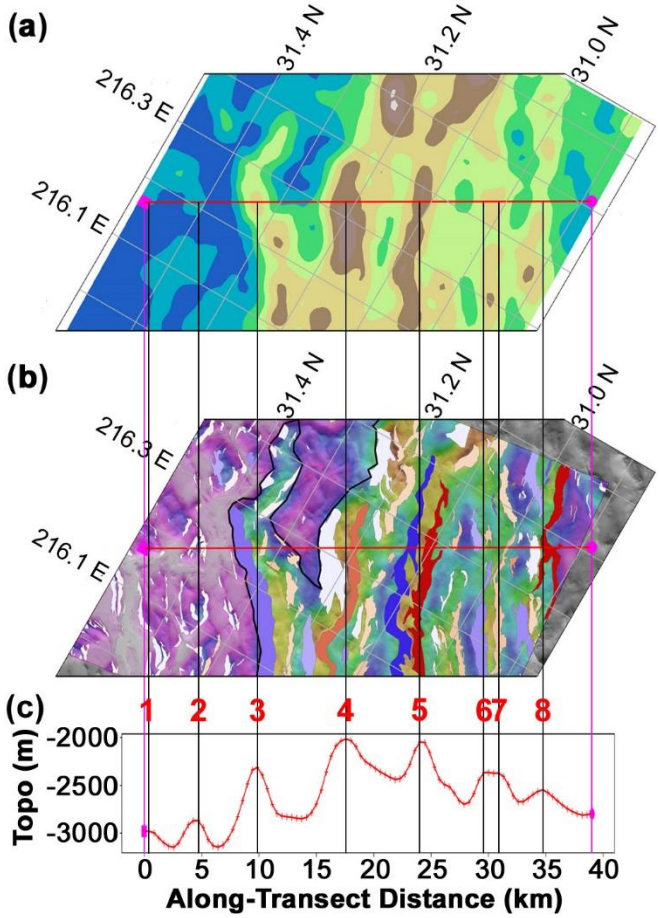

Figure 18. For the mesoscale analysis pertaining to the central profile line, the context plots include: **(a)** model topography, **(b)** total SS density **(Fig. 7)**, and **(c)** topographic profile. Black and magenta vertical lines denote topographic highs and the start/end of the profile, respectively, and are labeled with red numbers in panel **(c)**. These topographic highs are also displayed in **Figs 19, S13, & S14**.

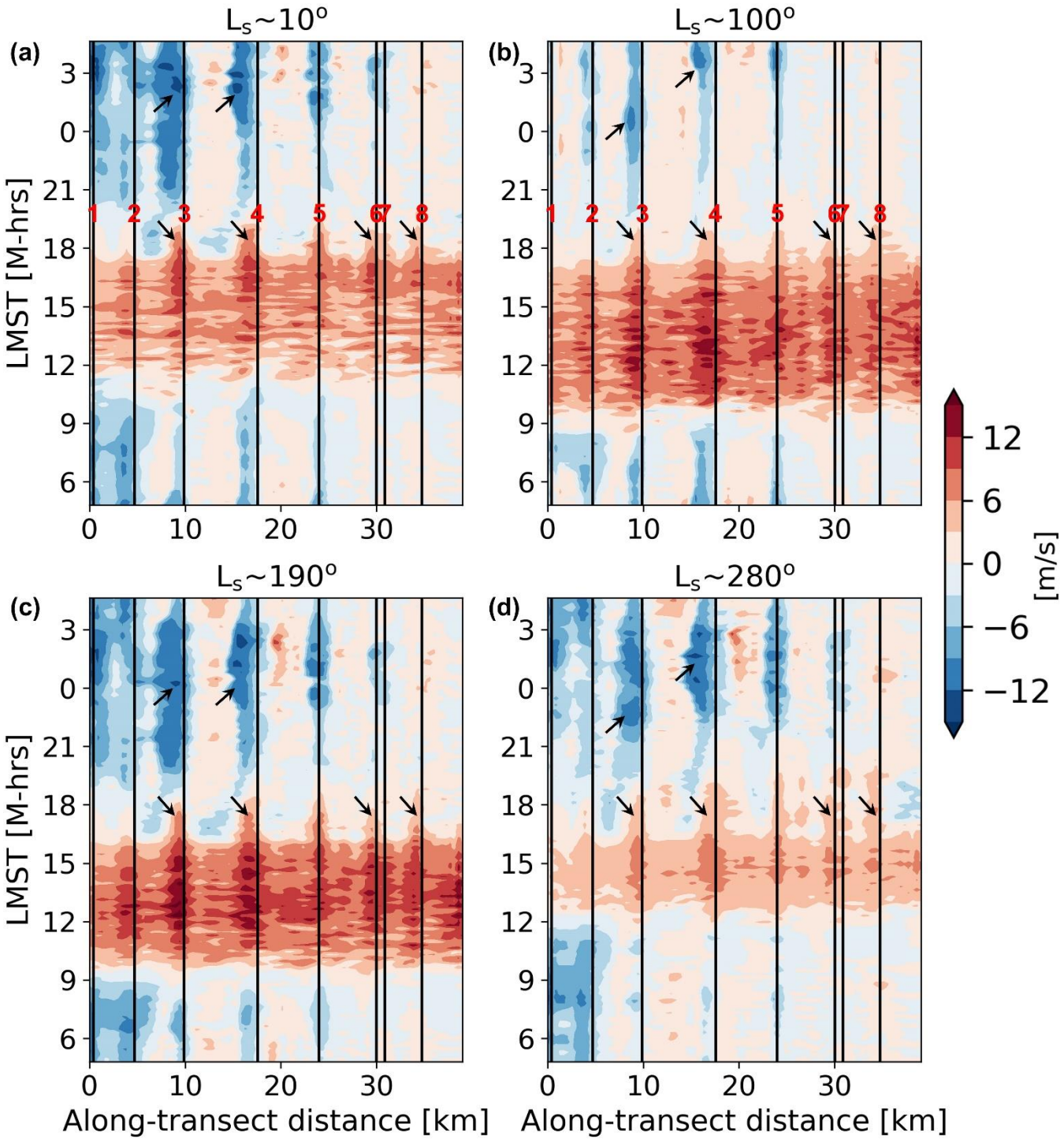

Figure 19. The Hovmuller plot illustrates wind speeds at 5 meters above ground level projected along the central profile (bearing of 153.5° or SSE; **Fig. 17 & 18**) as a function of season and Local Mean Solar Time (LMST). Panels **(a)** and **(c)** display wind speeds during the SS formation-enhanced equinox seasons, while panels **(b)** and **(d)** depict wind speeds during the SS formation-diminished solstice seasons. Arrows emphasize enhancements in wind speed on NW-facing slopes. Black vertical lines denote local topographic highs along the transect.

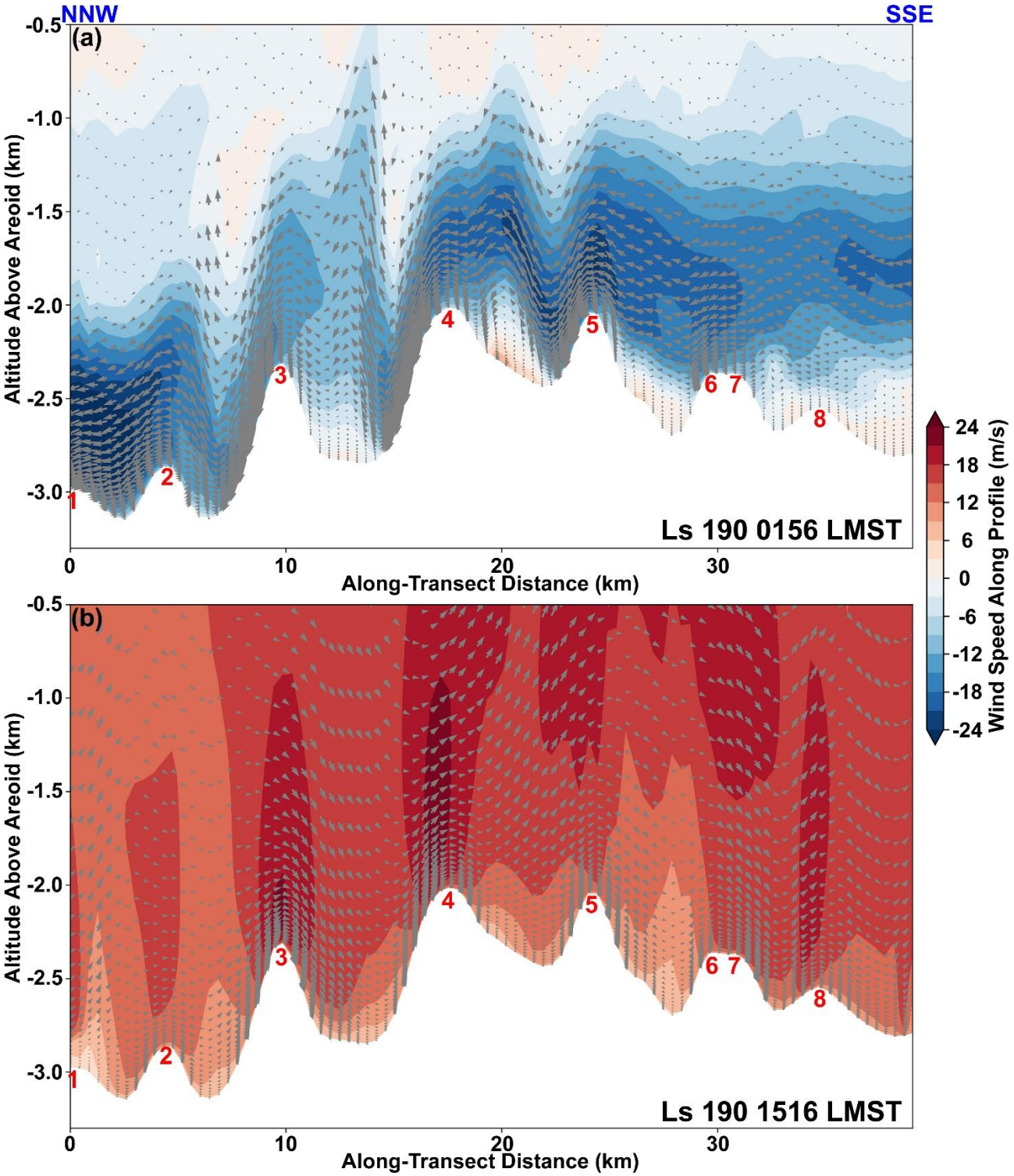

Figure 20. (a) Nighttime and **(b)** daytime wind speeds projected along the central profile (**Fig. 17 & 18**) as a function of altitude with the topographic highs labeled. During nighttime, a low-level jet is modeled at an altitude of -1.5 to -2.0 km at large transect distances. This jet leaves a quiescent zone below, facilitating the deposition of dust in the absence of strong winds. Notably, strong winds descend to near the surface on the NW-facing slopes of ridges 3, 4, and 5. Conversely, daytime winds remain relatively

constant across the length of the profile and at altitude, primarily due to boundary layer mixing and convection. Vertical exaggeration is 8.7 and LMST is the Local Mean Solar Time.

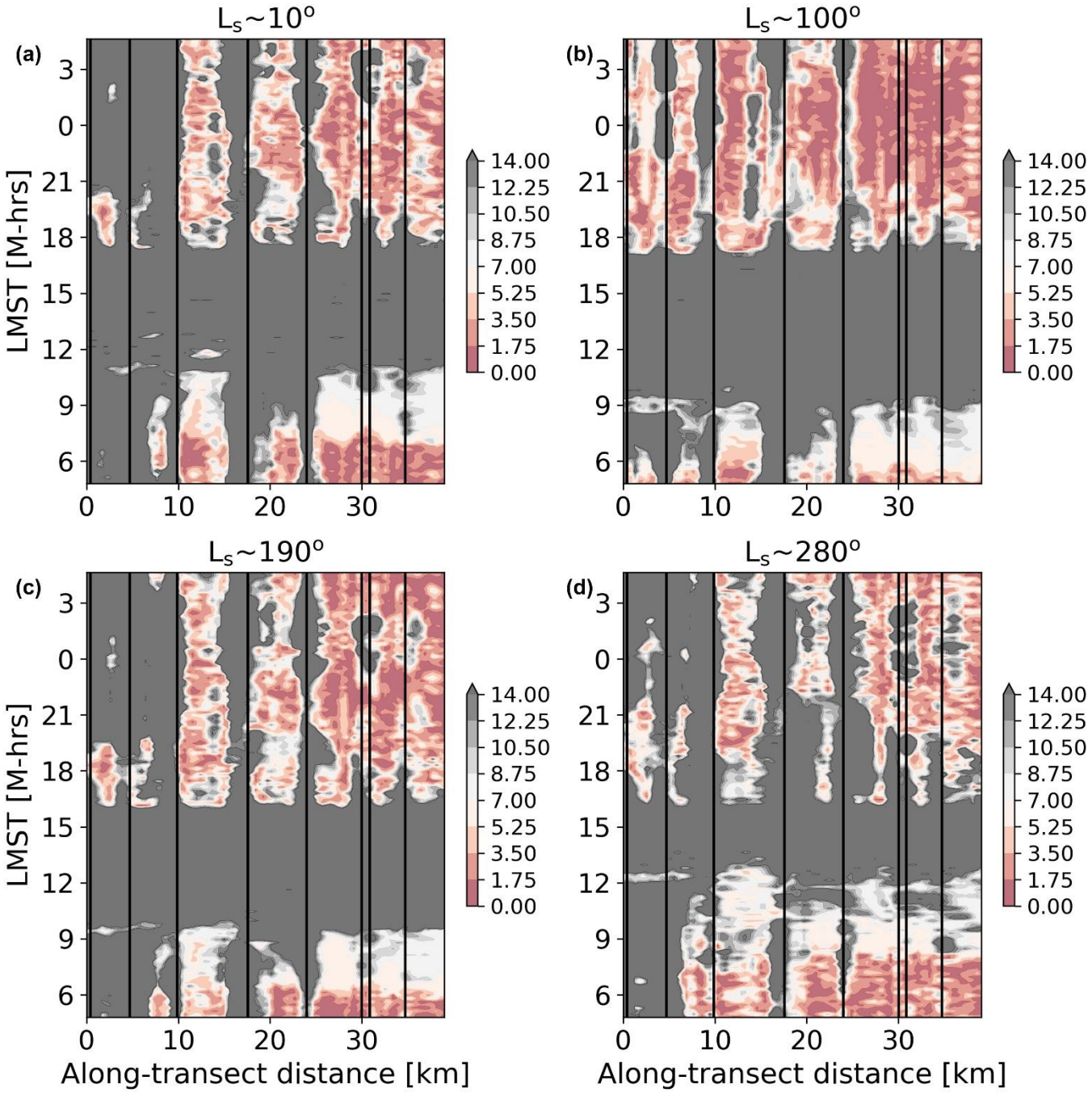

Figure 21. Variations in *u** (frictional velocity in m/s) values across seasons and times of day reveal significant differences. Dust remains suspended for *u** values exceeding 7 (*White et al.,* 1997), suggesting a lower likelihood of dust settling during daytime and on the ridges near 0 and 5 km along the transect. We adopt a mean fall speed of 0.011 m/s for a dust particle with a radius of 5 μm and a density of 2700 kg m^{-3}. LMST denotes Local Mean Solar Time.

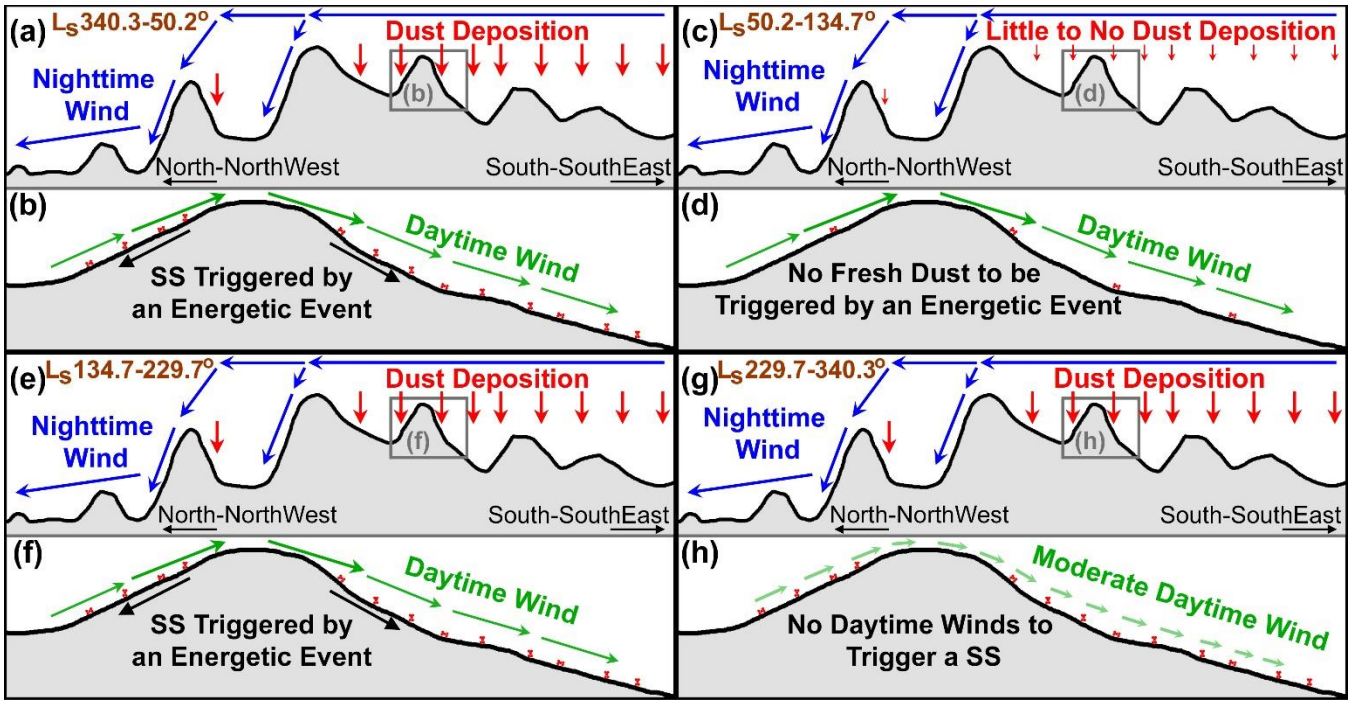

Figure 22. Cartoon illustrating our hypothesis of the SS recharge and formation processes as a function of season. **(a,c,e,g)** Notable downsloping nighttime winds occur on NW-facing slopes due to high ridges followed by deep valleys. These winds limit dust deposition on these slopes (**Figs. 19-21**). Dust tends to accumulate along other NW- and almost all SE-facing slopes, except during the northern summer season **(c)**, characterized by the lowest atmospheric opacity. **(b,f)** Newly-deposited dust can be triggered into SS by energetic events. We propose that an important trigger is the momentum transfer from downslope (SE-facing slopes) daytime winds onto the surface (**Figs. 19-21**). Upslope winds mainly affect NW-facing slopes, where occurrences of slope streaks (SS) are notably lower—approximately 7.6 times less frequent compared to other slopes. While daytime upslope winds would trigger SS, they are observed to be less effective at initiating these flows. **(c and d)** While daytime winds are robust, the absence of fresh dust agglomerates impedes the triggering the SS flows. **(g and h)** Moderate daytime winds lack the necessary strength to initiate flows, even in the presence of overnight fresh dust deposition.